

**A Defective Thesis: Studying the Behaviour of Defects in  
Liquid-Crystalline Materials**

by

**A. A. S. Green**

B.Sc., University of Calgary 2011

M.S., University of Colorado at Boulder 2015

A thesis submitted to the  
Faculty of the Graduate School of the  
University of Colorado in partial fulfillment  
of the requirements for the degree of  
Doctor of Philosophy  
Department of Physics  
2019

This thesis entitled:  
A Defective Thesis: Studying the Behaviour of Defects in Liquid-Crystalline Materials  
written by A. A. S. Green  
has been approved for the Department of Physics

---

Prof. Noel Clark

---

Professor Leo Rhadzihofsky

---

Professor David Walba

Date \_\_\_\_\_

The final copy of this thesis has been examined by the signatories, and we find that both the content and the form meet acceptable presentation standards of scholarly work in the above mentioned discipline.

Green, A. A. S. (Ph.D., Physics)

A Defective Thesis: Studying the Behaviour of Defects in Liquid-Crystalline Materials

Thesis directed by Prof. Noel Clark

## **Dedication**

To my parents.

## Acknowledgements

Here's where you acknowledge folks who helped. But keep it short, i.e., no more than one page, as required by the Grad School Specifications.

## Contents

### Chapter

<b>1</b>	<b>Introduction</b>	<b>1</b>
1.1	Liquid Crystals . . . . .	1
1.1.1	Phases of matter . . . . .	1
1.1.2	The Rod Liquid Crystal . . . . .	1
1.1.3	The Bent Liquid Crystal . . . . .	1
1.1.4	Characterization of Liquid Crystals: Case Study . . . . .	1
1.2	Fluid Dynamics . . . . .	1
1.3	Fluid Dynamics of Liquid Crystals . . . . .	1
<b>2</b>	<b>The Discovery of Helicity in Tilted Bent-Core Smectics: <math>\text{Sm}(\text{CP})_\alpha</math></b>	<b>2</b>
2.1	Characterization of PAL30 . . . . .	3
2.1.1	Experimental Details . . . . .	4
2.1.2	Differential Scanning Calorimetry of PAL30 . . . . .	5
2.1.3	X-ray Scattering of PAL30 . . . . .	7
2.1.4	Optical Textures . . . . .	12
2.1.5	Polarization Current . . . . .	16
2.2	Results and Discussion . . . . .	19
<b>3</b>	<b>Future Work: Structure-Property in the PAL30 Homologous Series of Molecules</b>	<b>21</b>
3.1	The $\text{Sm}(\text{CP})_\alpha$ Phase: Smectic Chirality Beyond the B2 Phase . . . . .	22

3.2	The bent-core de Vries phase . . . . .	22
3.2.1	Textures of bent-code de Vries phase . . . . .	28
3.2.2	Electro-optics of bent-core de Vries phase . . . . .	28
3.2.3	X-ray analysis of bent-core de Vries phase . . . . .	28
3.3	Discussion for the bent-core de Vries phase . . . . .	28
3.4	Alignment-Induced Phase Transitions . . . . .	28
<b>4</b>	<b>Metrology Applications of Fluid Crystals</b>	<b>36</b>
4.1	Experimental Design . . . . .	36
4.2	Theory and Simulation . . . . .	39
4.3	Results and Discussion . . . . .	43

## Appendix

**Tables****Table**

## Figures

## Figure

2.1 Experimental characterization of PAL30. (a) The PAL30 molecule, showing the all-trans length calculated using the program Spartan. (b–d) Phase properties vs. temperature. The solid vertical lines denote phase boundaries and the cross-hatching phase coexistence. (b) SAXS shows the smectic layer spacing in all phases to be  $d_0 \approx 48 \text{ \AA}$ . Resonant carbon K-edge reflections are from superlayer modulations of the molecular orientation about the layer normal  $z$ , the peak at  $d_H \approx 150 \text{ \AA}$  corresponding to the pitch of the incommensurate, helical precession in the Sm2 phase, and at  $d_B = 2d_0$  to the bilayer ordering of the Sm3 and Sm4 phases. (c) Birefringence of planar-aligned cells with layers normal to the plates, with and without applied electric field ( $E = 20 \text{ V}/\mu\text{m}$ ). (d) Polarization current (in nA) in response to a triangle-wave applied electric field: a single-peak, Langevin-like response at lower temperatures in the Sm1 phase; a triple peak in the Sm2 phase, associated with ferrielectric switching[?] and indicative of helical unwinding[?], coalescing into a double peak in the Sm3, indicating a non-polar ground state at  $E = 0$ ; and a single current peak in the Sm4 phase caused by the block polarization switching of the ferroelectric Sm<sub>C<sub>A</sub></sub>P<sub>F</sub> ground state. (e–m) Characteristic optical textures in a planar cell, viewed between crossed polarizers. The  $E = 0$  textures are focal conics typical of a fluid smectic with an optic axis along  $z$ . Field application induces chiral, tilted conglomerate domains (of opposite handedness) in the Sm1–Sm3 phases, but only a change in birefringence in the Sm4. (n–q) Proposed superlayer structure of PAL30 phases, with and without applied electric field: (n) Sm1: achiral de Vries-like SmA → chiral Sm<sub>C<sub>S</sub></sub>P<sub>F</sub>; Sm2: superlayer chiral helix → chiral Sm<sub>C<sub>S</sub></sub>P<sub>F</sub>; Sm3: superlayer chiral bilayer Sm<sub>C<sub>A</sub></sub>P<sub>A</sub> → chiral Sm<sub>C<sub>S</sub></sub>P<sub>F</sub>; Sm4: Sm<sub>C<sub>A</sub></sub>P<sub>F</sub> with  $\mathbf{P}$  parallel to the glass → Sm<sub>C<sub>A</sub></sub>P<sub>F</sub> with  $\mathbf{P}$  normal to the glass.

2.2	Differential scanning calorimetry of PAL30. On cooling, there is only a small, enthalpy peak at $\approx 110^\circ\text{C}$ corresponding to the transition from the highest-temperature smectic phase, the Sm1, and the Sm2. . . . .	7
2.3	X-ray scattering of high temperature phase, Sm1, of $\text{Sm}(\text{CP})_\alpha$ . (a) The smectic layer size, $d$ , increases monotonically on cooling, with no inflection points that would be characteristic of a untilted $\rightarrow$ tilted phase transition. (b) No resonant scattering is observed for this phase. . . . .	8
2.4	Temperature behaviour of the $\text{Sm}(\text{CP})_\alpha$ phase plotted as a waterfall plot in (a), and as a contour plot in (b). A bilayer ( $d = 112 \text{ \AA} = 2d_0$ ) corresponds to the 2-layer unit-cell structure of the $\text{SmC}_\text{A}P_\text{A}$ phase, which sits directly below the $\text{Sm}(\text{CP})_\alpha$ phase in temperature. The resonant peak corresponding to the $\text{Sm}(\text{CP})_\alpha$ phase at $d \approx 150 \text{ \AA}$ is direct evidence that the $\text{Sm}(\text{CP})_\alpha$ phase is not a classic B2-type phase. . . . .	9
2.5	X-ray scattering from PAL30. (a) SAXS gives a peak from the smectic layer ordering at $q = q_0$ . The RSoXS peak at $q_H$ indicates that there is superlayer orientational ordering with periodicity $d_H$ in the Sm2 phase. In general, superlayer orientational modulation in a smectic generates RSoXS peaks at wavevectors along the layer normal at $q(l, m) = l(2\pi/d_0) \pm m(2\pi/d_H)$ [?]. The observation of an RSoXS reflection at $q = q(0, 1)$ and the absence of an Umklapp peak at $q = q(1, -1)$ in the Sm2 confirms a superlayer helix with a scattering amplitude modulation due to the smectic layering that is undetectably weak. (b) Temperature dependence of resonant scattering. The helix peak at $q_H \approx 1/(2.8d_0)$ becomes diffuse in the Sm3 phase. Splitting of the bilayer peak at $q_B$ , which would indicate helical precession of the bilayer structure, is not observed. . . . .	11
2.6	Planar aligned textures of Sm1. (a) Applied field out of the page, (b) ground state (no field), (c) applied field into the page. . . . .	12

2.7 Optical tilt of PAL30 vs. applied field. The Sm1 phase shows no electrooptic response in weak fields $E < E_{\text{th}}$ . Fields $E > E_{\text{th}}$ induce an electroclinic tilt and result in the formation of chiral domains. $E_{\text{th}}$ , which becomes smaller with decreasing $T$ (inset), matches closely $E_{\text{sat}}$ , the field at which the induced polarization saturates, extracted from Figure 2.1(d). The Sm2 phase exhibits a chiral electroclinic effect near $E = 0$ and hysteresis in the field-induced helix unwinding to the $\text{SmC}_S P_F$ state. . . . .	13
2.8 Calculated birefringence of PAL30, assuming Boulder phase assignments, shown as a function of temperature . . . . .	14
2.9 Textures of both the Sm2 ( $\text{Sm}(\text{CP})_\alpha$ ) and Sm3 ( $\text{SmC}_A P_A$ ) phases of PAL30: reminiscent of a $\text{SmC}_A P_A$ texture. . . . .	15
2.10 Textures of both the Sm2 ( $\text{Sm}(\text{CP})_\alpha$ ) and Sm3 ( $\text{SmC}_A P_A$ ) phases of PAL30: reminiscent of a $\text{SmC}_A P_A$ texture. . . . .	15
2.11 Polarization current of PAL30 shown as a function of the applied field strength. . . . .	16
2.12 Zoomed in polarization current measurements for PAL30 in the high temperature Sm1 phase. . . . .	17
2.13 The polarization current and the optical tilt plotted as a function of applied field strength for both the Sm1 (de Vries SmA) (a,b) and the Sm2 ( $\text{Sm}(\text{CP})_\alpha$ ) (c-d). The polarization current has additionally been integrated to calculate the time-dependant net polarization. The threshold electric field ( $E_{\text{th}}$ ) required to manifest the tiger-stripes can be directly read from the green curve denoting the optical tilt (for $T=110^\circ\text{C}$ , $E_{\text{th}} \approx 5 \text{ V}/\mu\text{m}$ ), and the saturation electric field where the net polarization is no longer changing ( $E_{\text{sat}}$ ) can be directly read from the red curve, which denotes the net polarization, (for $T=110^\circ\text{C}$ , $E_{\text{sat}} \approx 5 \text{ V}/\mu\text{m}$ ). Both $E_{\text{th}}$ and $E_{\text{sat}}$ are plotted in as the inset of Figure 2.7. . . . .	17
2.14 Polarization current of sm2 of PAL30 plotted against applied voltage . . . . .	18

2.15	Polarization current measurements for PAL30 in the high temperature Sm1 phase. . . . .	19
2.16	Evolution of de Vries SmA bent-core phase under the application of a field . . . . .	20
3.1	The polarization current and the optical tilt plotted as a function of applied field strength for both the Sm1 (de Vries SmA) (a,b) and the Sm2 ( $\text{Sm}(\text{CP})_\alpha$ ) (c-d). The polarization current has additionally been integrated to calculate the time-dependant net polarization. The threshold electric field ( $E_{\text{th}}$ ) required to manifest the tiger-stripes can be directly read from the green curve denoting the optical tilt (for $T=110^\circ\text{C}$ , $E_{\text{th}} \approx 5 \text{ V}/\mu\text{m}$ ), and the saturation electric field where the net polarization is no longer changing ( $E_{\text{sat}}$ ) can be directly read from the red curve, which denotes the net polarization, (for $T=110^\circ\text{C}$ , $E_{\text{sat}} \approx 5 \text{ V}/\mu\text{m}$ ). Both $E_{\text{th}}$ and $E_{\text{sat}}$ are plotted in as the inset of Figure 2.7. . . . .	24
3.2	Experimental data for ‘hockey-stick’ compound studied by Eremin et al.[?] Note, the threshold for optical tilt. The lines guide the only. . . . .	26
3.3	. . . . .	28
3.4	. . . . .	29
3.5	. . . . .	29
3.6	. . . . .	30
3.7	. . . . .	31
3.8	. . . . .	31

3.9 Planar textures of <b>n-16</b> at approximately 116 °C in an LC vision cell (a-c) and an Instec cell (d-f) viewed under cross polarizers. Both cells use a polyimide anti-parallel alignment layer. The LC vision cell has clear focal conics, while the Instec cell is entirely aligned. Both textures manifest chirality, seen as the distinct difference between the textures with a negative or positive out-of-plane electric field applied. The contrast between handed domains shows up clearly in the LC vision cells (compare (g) and (i)) while the contrast in the Instec cells is barely distinguishable. . . . .	32
3.10 Planar textures of <b>n-16</b> at approximately 110 °C in an LC vision cell (a-c) and an Instec cell (d-f) viewed under cross polarizers. Both cells use a polyimide anti-parallel alignment layer. The LC vision cell has clear focal conics, while the Instec cell is entirely aligned. Both textures manifest chirality, seen as the distinct difference between the textures with a negative or positive out-of-plane electric field applied. The contrast between handed domains shows up clearly in the LC vision cells (compare (g) and (i)) while the contrast in the Instec cells is barely distinguishable. . . . .	34
3.11 Planar textures of <b>n-16</b> at approximately 100 °C in an LC vision cell (a-c) and an Instec cell (d-f) viewed under cross polarizers. Both cells use a polyimide anti-parallel alignment layer. The LC vision cell has clear focal conics, while the Instec cell is entirely aligned. Both textures manifest chirality, seen as the distinct difference between the textures with a negative or positive out-of-plane electric field applied. The contrast between handed domains shows up clearly in the LC vision cells (compare (g) and (i)) while the contrast in the Instec cells is barely distinguishable. . . . .	35

4.1 Smectic film flow meter geometry. (a) A stainless steel film holder ( $45.2\text{ mm} \times 34.8\text{ mm} \times 7.6\text{ mm}$ ) has a $w = 3.1\text{ mm}$ -wide channel in the form of a racetrack cut to a depth $h = 3.7\text{ mm}$ . At viewing ports centered along each ‘arm’, the channel is cut all the way through the film holder (a depth of $7.6\text{ mm}$ ). Gas is coupled into and out of the system by means of co-linear, $2\text{ mm}$ -diameter holes at the ends of the film holder. Smectic films are created by coating the bottom of a glass coverslip (the spreader) with liquid crystal material and drawing it across the top opening of the channel. The film is shielded from random air currents from above by a sealed cover (not shown). The photomicrograph shows typical islands (localized regions with more layers than the background film) used to track flow of the film in one of the viewing regions of the racetrack. (b) Schematic cross-section of a smectic film suspended across the channel (not to scale). The film comprises an integer number of smectic layers and can be as thin as two molecules ( $\sim 6\text{ nm}$ ). In general, a meniscus forms where the film contacts the edges of the channel. . . . .	37
4.2 Analytic analysis of symmetric, two-phase, stratified fluid flow in an infinitely long pipe of width $a$ . (a) Ratio between the average film and air velocities as a function of the phase fraction (the ratio of the volume of the fluid and the volume of the air, $\phi = h_{\text{film}}/h_{\text{air}}$ ). When the phase fraction is very small, the film is strongly coupled to the air and moves with the same speed. (b) Flow velocity in the top half of the pipe. At left, both air and film are flowing through the pipe (the blue dashed line demarcates the upper boundary of the film), while on the right only air is present. The $y$ dimension is scaled by the half the thickness of the LC film, $h_{\text{film}}$ . The flow fields in these two cases are practically indistinguishable, suggesting that the influence of the LC film on the airflow is negligible. . . . .	40

4.3 Computed airflow in the racetrack geometry. (a) Model velocity field for inlet velocity $v_{\text{inlet}} = 0.15 \text{ m/s}$ . The air does not circulate uniformly in the same sense around the racetrack, instead splitting between the front and back legs. (b) Model velocity field for inlet velocity $v_{\text{inlet}} = 0.65 \text{ m/s}$ . Above a transition inlet velocity of $v_{\text{inlet}} = 0.55 \text{ m/s}$ , the air circulates uniformly around the racetrack. (c) Predicted net film speed ( $v_{\text{film}} \propto v_2 - v_1$ ) for a range of inlet velocities. The slope of this curve gives an average theoretical sensitivity of $S = 0.15$ . The background shading reflects the experimental observations with different inlet velocities: for $v_{\text{in}} < 0.3 \text{ m/s}$ , the film flow is chaotic; for $0.3 \text{ m/s} < v_{\text{in}} < 1.2 \text{ m/s}$ , the film exhibits stable Poiseuille flow; for $v_{\text{in}} > 1.2 \text{ m/s}$ , the film undergoes rapid out-of-plane oscillations that make particle tracking impractical. . . . .	42
4.4 Characterization of flow meter. (a) Velocity profiles over the width of the racetrack channel, with each point corresponding to a specific tracked island. The profiles are well described by parabolas (smooth curves), confirming Poiseuille flow over a wide-range of inlet velocities. At higher velocities, the data are noisier due to the relatively paucity of islands that can be captured in sequential frames. The left-right asymmetry in the number of measurements is an artifact due to defects on one side of the camera sensor. (b) Spatially averaged film velocity in the observation region as a function of inlet air velocity. Measurements were performed over four separate days, using more than 30 films. The volumetric flow rate of the air being injected into the racetrack through the inlet was measured using an independent mechanical sensor. The average film speed is linearly proportional to the speed of the air at the device inlet, with a sensitivity that is independent of flow rate. . . . .	44

## **Chapter 1**

### **Introduction**

## **1.1 Liquid Crystals**

### **1.1.1 Phases of matter**

### **1.1.2 The Rod Liquid Crystal**

### **1.1.3 The Bent Liquid Crystal**

### **1.1.4 Characterization of Liquid Crystals: Case Study**

## **1.2 Fluid Dynamics**

## **1.3 Fluid Dynamics of Liquid Crystals**

## Chapter 2

### The Discovery of Helicity in Tilted Bent-Core Smectics: $\text{Sm}(\text{CP})_\alpha$

The discovery of spontaneous macroscopic polar ordering [?] and chirality [?] in fluid smectic liquid crystal phases of achiral bent-core mesogens has led to the exploration of a rich family of novel liquid crystal phases and self-assemblies [?, ?, ?, ?, ?, ?] in which the key macroscopic elements of polarity, chirality, and smectic layering all appear as spontaneously broken symmetries. While the smectic layer-scale order of bent-core mesogens, resulting from strong intralayer coupling between molecular tilt and polarity, is quite well characterized, superlayer structuring beyond that of the four basic SmCP bilayer phases combining synclinic or anticlinic tilt with ferroelectric or antiferroelectric polarity [?], as sketched in Supplemental Figure S1, have not been definitively identified. Possible superlayer structures analogous to those seen in tilted  $\text{SmC}^*$  phases of chiral, rod-shaped molecules could be incommensurate or commensurate with the underlying smectic layer spacing and feature states of varying azimuthal orientation of the molecular long axis about the layer normal,  $z$ , such as the chiral helical precession along  $z$  with equal, discrete orientational jumps between layers of the  $\text{SmC}_\alpha^*$  phase and the ferrielectric phases with periodic arrays of discrete jumps of different sizes [?].

Since the period of such superlayer structures,  $p$ , can be as short as two layers, the structural study of such phases requires the effective probing of molecular orientation at the nanoscale. This can be achieved using resonant X-ray scattering, a technique sensitive to

put  
joe  
prc in  
begin-  
ning  
of sub-  
sec-  
tion

put  
biref/tilt  
figure  
in the  
optical  
textures/ele  
optics  
sec-  
tion

atomic environment [?, ?, ?, ?, ?, ?, ?, ?, ?, ?, ?] that has previously enabled the discovery and definitive characterization of superlayer organization in several SmC\* phases and sub-phases, employing the K-edge resonance of atoms incorporated in the liquid crystal molecule [?, ?].

Several recent observations suggest the possibility of chiral superlayer ordering in achiral bent-core mesogens: Takanishi et al. have identified such a structure in a SmCP phase of a bent-core mesogen doped with a chiral, rod-shaped molecule that as a neat material exhibits SmC $_{\alpha}^*$  and ferrielectric phases [?]; Abberley et al. have reported a superlayer helix in a smectic phase of bent dimers of molecular rods [?]; Panarin and co-workers have recently proposed, based on AFM evidence, the existence of tilted, helical supermolecular ordering in several achiral bent-core mesogens with 4-cyanoresorcinol bisbenzoate cores [?]. Earlier investigations of this molecular family had concluded, however, that their polar phases were orthogonal, i.e., untilted and therefore not chiral [?, ?]. Motivated by these conflicting reports and the ongoing interest in the chiral sub-phases of liquid crystals, we have studied one of the members of this homologous series, PAL30, which has  $n = 14$  alkyl tails (see Figure 2.1(a)). Our experiments, using non-resonant X-ray scattering (SAXS), resonant soft X-ray scattering (RSoXS), electro-optic techniques, and polarized light microscopy (PLM), summarized in Figure 2.1, reveal an exotic phase sequence, including an achiral de Vries smectic which becomes chiral in sufficiently large applied electric fields, and, at lower temperature, a tilted, chiral smectic with superlayer helical ordering.

## 2.1 Characterization of PAL30

We used a combination of two-dimensional, small-angle, hard X-ray scattering (SAXS), resonant, soft X-ray scattering (RSoXS), differential scanning calorimetry (DSC), polarized, transmitted light microscopy on cells in transmission, and measurements of the polarization reversal current of cells in order to characterize PAL30. These experiments reveal four smectic phases, labeled in order of descending temperature as Sm1, Sm2, Sm3, and Sm4.

### 2.1.1 Experimental Details

The RSoXS experiments were performed at the Advanced Light Source at Lawrence Berkeley National Laboratory beamline 11.0.1.2 using linearly polarized X-ray photons [?, ?]. The X-ray energy was tuned between 270 eV and 290 eV in our experiments, with scattering contrast appearing only for energies near the carbon K-edge resonance ( $E = 284$  eV), indicating the presence of real-space features with an orientational modulation. The PAL30 material was sandwiched between two silicon nitride substrates, while in the isotropic phase. The cell was then placed into a temperature controlled hotstage in the beamline. After finding the highest temperature where scattering features were observed, the sample was cooled slowly while recording 2D diffractograms of the scattering. The RSoXS setup is sensitive to orientational modulations from  $d = 50$  Å to 1250 Å. The relative positions and orientations of the sample and detector were calibrated using a sample with known scattering  $q$ -values. The data from the detector was processed using the Igor Pro-based NIKA data reduction software package [?, ?].

The angular resolution of the diffractometer, estimated from the full width at half-maximum of a resonant feature known to be twice the smectic layer spacing is  $\delta q \sim 0.000\,78\text{ \AA}^{-1}$ .

SAXS measurements were carried out on beamline X10A of the National Synchrotron Light Source (NSLS), at Brookhaven National Laboratory. This beamline has a Si 111 double monochromator, tuned to around 10 keV. The sample was mounted in an Instec hot stage on a Huber four-circle goniometer. The angular resolution of the diffractometer, measured by scanning the detector arm through the attenuated direct beam, is  $\delta q \sim 0.005\text{ nm}^{-1}$  full width at half-maximum.

The planar cells used for texture analysis were 4.5 μm thick commercial cells purchased from Instec Inc. with rubbed polyimide planar alignment layers and ITO glass. The thickness of the empty cells was measured using a visible light spectrometer. The cells were then filled

with PAL30 in the isotropic phase. Polarization reversal current was measured in these cells by applying an alternating, triangular voltage.

The birefringence was measured using a Zeiss quartz-wedge compensator and a 5.86  $\mu\text{m}$  thick Instec cell.

The molecular length of PAL30 was estimated using a Hartree-Fock 6-31G\* calculation of a single molecule in the gas phase using the Spartan  $\ddot{\text{A}}\ddot{\text{Y}}16$  numerical calculation package.

### 2.1.2 Differential Scanning Calorimetry of PAL30

The DSC reveals only a single enthalpy peak on cooling, at approximately 110  $^{\circ}\text{C}$ , hinting that the Sm1  $\rightarrow$  Sm2 transition is either a weakly first order, or a second order transition.

The lack of other enthalpy peaks is concerning, considering we identify four unique smectic phases in the phase sequence of PAL30. However, the resonant scattering experiments described in [subsection 2.1.3](#), particularly the soft-melting mode seen in [Figures 2.4](#), shows that the phase transition from the Sm2  $\rightarrow$  Sm3 is strongly second order, spanning a temperature range of 10  $^{\circ}\text{C}$ , which explains the absence of a distinct enthalpy peak in the DSC for this transition

The lack of a distinct peak for the Sm3  $\rightarrow$  Sm4 peak has two plausible explanations. First, the polarization current shown in ?? shows that the transition is likely second order, spanning a temperature range of approximately 5  $^{\circ}\text{C}$ , like the Sm2  $\rightarrow$  Sm3. Though, as the identified structures of the Sm3 ( $\text{SmC}_\text{A}P_\text{A}$ ) and Sm4 ( $\text{SmC}_\text{A}P_\text{F}$ ) cannot be connected by a continuous deformation the same way the helical Sm2 ( $\text{Sm}(\text{CP})_\alpha$ ) can be deformed into the Sm2 ( $\text{SmC}_\text{A}P_\text{A}$ ), this seems less likely.

The other explanation, which I consider more likely, is due to the fact the DSC is measured without a field present, raising the possibility first explored by Guzman[?] for orthogonal phases, that the transition from the  $\text{SmC}_\text{A}P_\text{A}$  to the  $\text{SmC}_\text{A}P_\text{F}$  could be a kinetic

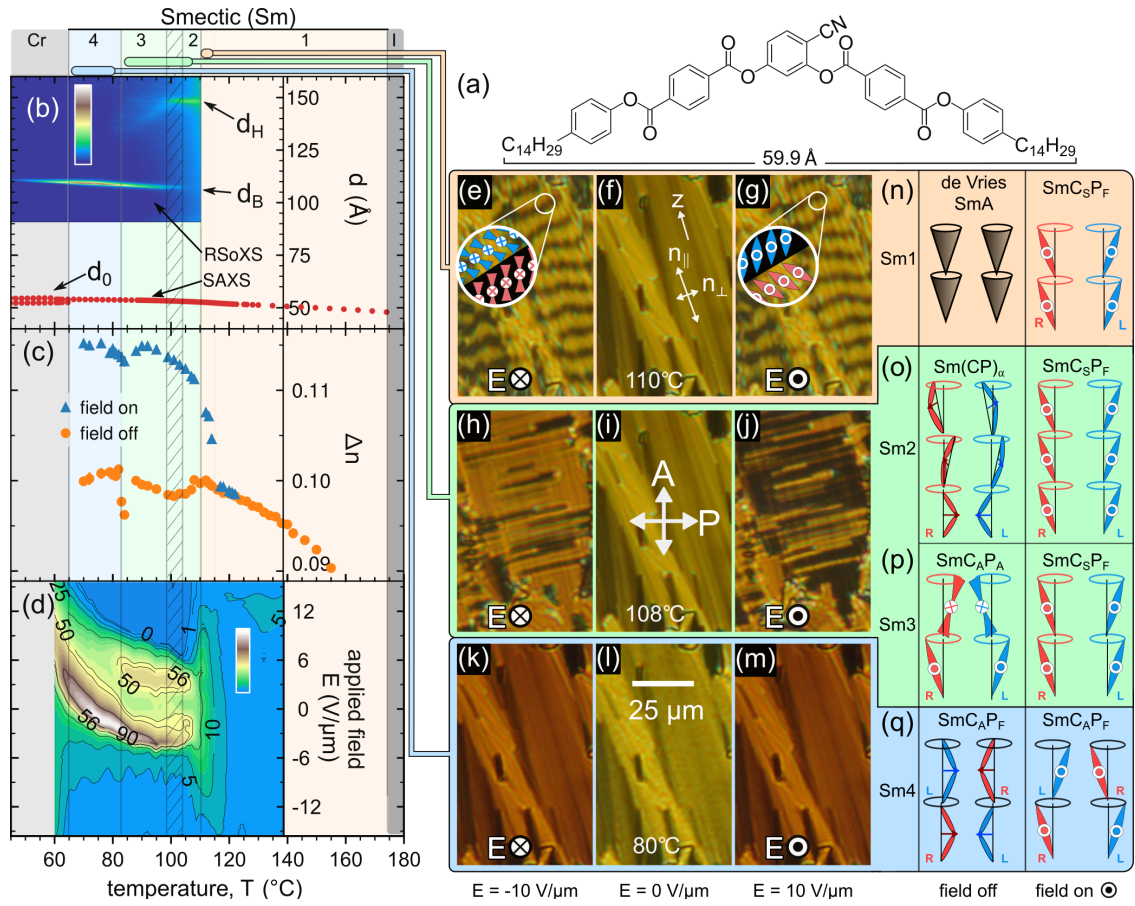


Figure 2.1: Experimental characterization of PAL30. (a) The PAL30 molecule, showing the all-trans length calculated using the program Spartan. (b–d) Phase properties vs. temperature. The solid vertical lines denote phase boundaries and the cross-hatching phase coexistence. (b) SAXS shows the smectic layer spacing in all phases to be  $d_0 \approx 48 \text{ \AA}$ . Resonant carbon K-edge reflections are from superlayer modulations of the molecular orientation about the layer normal  $z$ , the peak at  $d_H \approx 150 \text{ \AA}$  corresponding to the pitch of the incommensurate, helical precession in the Sm2 phase, and at  $d_B = 2d_0$  to the bilayer ordering of the Sm3 and Sm4 phases. (c) Birefringence of planar-aligned cells with layers normal to the plates, with and without applied electric field ( $E = 20 \text{ V}/\mu\text{m}$ ). (d) Polarization current (in nA) in response to a triangle-wave applied electric field: a single-peak, Langevin-like response at lower temperatures in the Sm1 phase; a triple peak in the Sm2 phase, associated with ferrielectric switching[?] and indicative of helical unwinding[?], coalescing into a double peak in the Sm3, indicating a non-polar ground state at  $E = 0$ ; and a single current peak in the Sm4 phase caused by the block polarization switching of the ferroelectric SmC<sub>A</sub>P<sub>F</sub> ground state. (e–m) Characteristic optical textures in a planar cell, viewed between crossed polarizers. The  $E = 0$  textures are focal conics typical of a fluid smectic with an optic axis along  $z$ . Field application induces chiral, tilted conglomerate domains (of opposite handedness) in the Sm1–Sm3 phases, but only a change in birefringence in the Sm4. (n–q) Proposed superlayer structure of PAL30 phases, with and without applied electric field: (n) Sm1: achiral de Vries-like SmA → chiral SmC<sub>S</sub>P<sub>F</sub>; Sm2: superlayer chiral helix → chiral SmC<sub>S</sub>P<sub>F</sub>; Sm3: superlayer chiral bilayer SmC<sub>A</sub>P<sub>A</sub> → chiral SmC<sub>S</sub>P<sub>F</sub>; Sm4: SmC<sub>A</sub>P<sub>F</sub> with **P** parallel to the glass → SmC<sub>A</sub>P<sub>F</sub> with **P** normal to the glass.

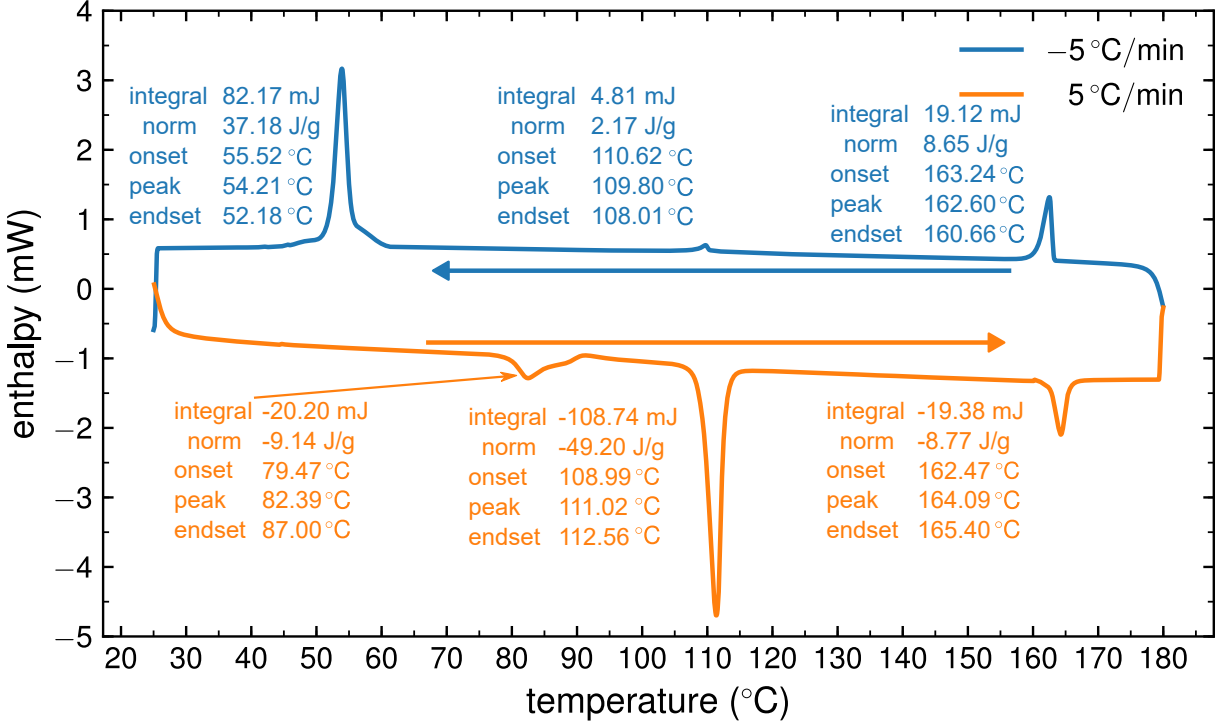


Figure 2.2: Differential scanning calorimetry of PAL30. On cooling, there is only a small, enthalpy peak at  $\approx 110^\circ\text{C}$  corresponding to the transition from the highest-temperature smectic phase, the Sm1, and the Sm2.

trap. If this was the case, then the  $\text{SmC}_A P_A$  would be expected to be the ground-state phase *in absence of an applied field* for the remainder of the phase sequence. This could be tested in future experiments with the DC hysteresis measurements described in Dr. Guzman's thesis[?].

### 2.1.3 X-ray Scattering of PAL30

X-ray scattering from PAL30 is shown in Figures 2.1(b) and S3.

Upon cooling from the isotropic, a single, non-resonant SAXS peak appears at  $175^\circ\text{C}$ , at a wavevector  $q_0$  corresponding to Bragg scattering from the smectic layers in the Sm1 phase with spacing  $d_0 = 2\pi/q_0 = 48\text{\AA}$ .

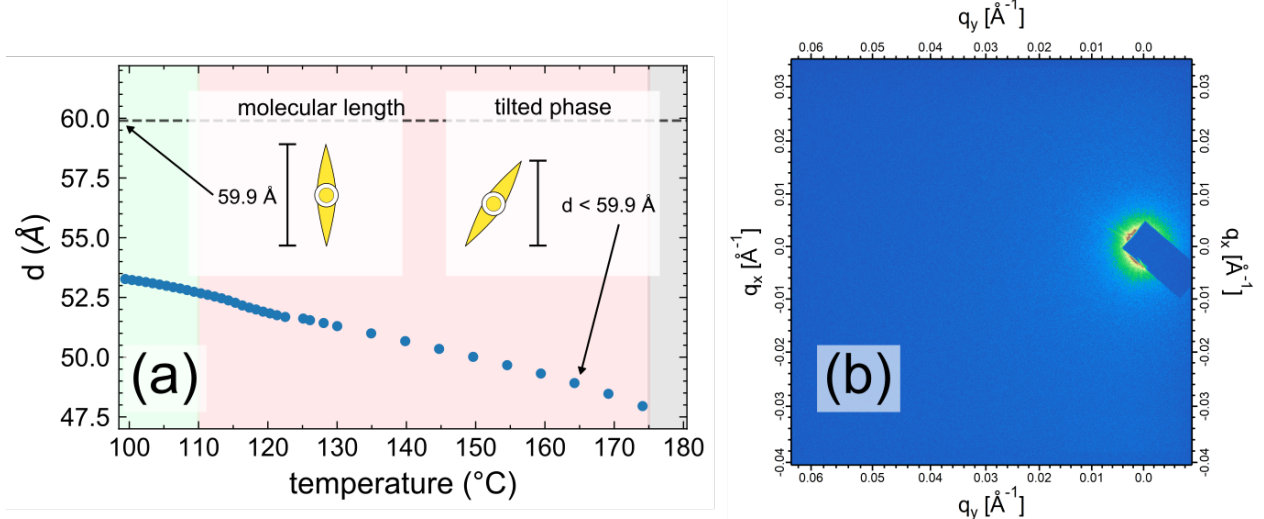


Figure 2.3: X-ray scattering of high temperature phase, Sm1, of  $\text{Sm}(\text{CP})_\alpha$ . (a) The smectic layer size,  $d$ , increases monotonically on cooling, with no inflection points that would be characteristic of a untilted $\rightarrow$ tilted phase transition. (b) No resonant scattering is observed for this phase.

The layer spacing increases slightly on cooling to the crystal phase at  $65^\circ\text{C}$  and is consistently smaller than the calculated molecular length,  $l = 59.9 \text{ \AA}$ , throughout this temperature range, suggesting that the molecules are tilted in all of the smectic phases, to first order by an average amount estimated using  $\theta_{\text{xray}} = \cos(d_0/l)$  of  $33^\circ$  (see Figure S4). In the Sm1 temperature range ( $110^\circ\text{C} \leq T \leq 175^\circ\text{C}$ ), there are no RSoXS scattering features (Figure 2.3 (b)) that would indicate a superlayer periodic structure.

At the transition to the Sm2 phase, at  $110^\circ\text{C}$ , marked by a distinct enthalpy peak in the DSC (Figure S5), a single, sharp resonant peak appears at  $q_H = 0.042 \text{ \AA}^{-1}$ , corresponding to a molecular orientational structure with a period  $d_H = 148 \text{ \AA} \approx 2.8d_0$  that is incommensurate with the smectic layer spacing (Figure 2.5(b) and Figure 2.4). Below  $104^\circ\text{C}$ , this reflection becomes weaker and another sharp, resonant reflection at higher  $q$  grows in, the coexistence indicating a first-order transition to the Sm3 phase. This second Bragg peak, which persists down to the crystal phase, has a wavevector  $q_B \approx q_0/2$ , indicative of a commensurate, bilayer orientational structure in the Sm3 and Sm4 phases.

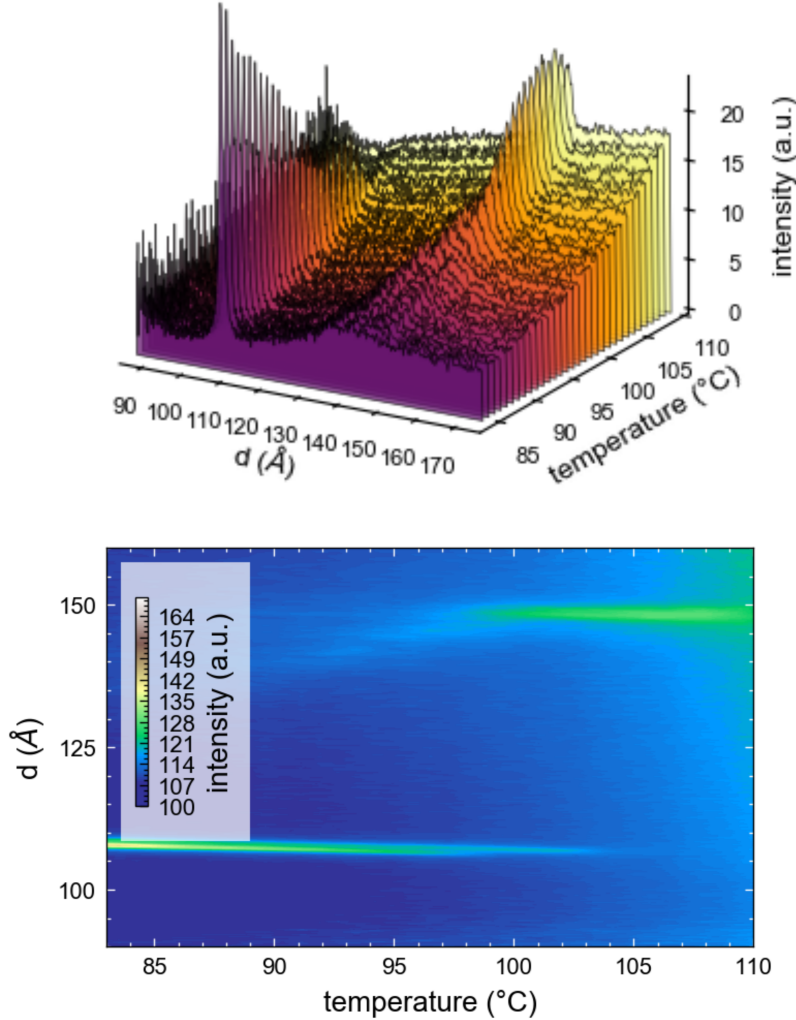


Figure 2.4: Temperature behaviour of the  $\text{Sm}(\text{CP})_\alpha$  phase plotted as a waterfall plot in (a), and as a contour plot in (b). A bilayer ( $d = 112 \text{ \AA} = 2d_0$ ) corresponds to the 2-layer unit-cell structure of the  $\text{SmCPA}$  phase, which sits directly below the  $\text{Sm}(\text{CP})_\alpha$  phase in temperature. The resonant peak corresponding to the  $\text{Sm}(\text{CP})_\alpha$  phase at  $d \approx 150 \text{ \AA}$  is direct evidence that the  $\text{Sm}(\text{CP})_\alpha$  phase is not a classic B2-type phase.

Below  $99^\circ\text{C}$ , the incommensurate peak broadens dramatically and moves to higher  $q$ , indicating the presence of short-ranged, Sm2-like helical fluctuations persisting in the Sm3 phase, and disappears at the transition to the Sm4 phase at  $83^\circ\text{C}$ . The Sm4 phase exhibits only the bilayer RSoXS reflection at  $q_B$ .

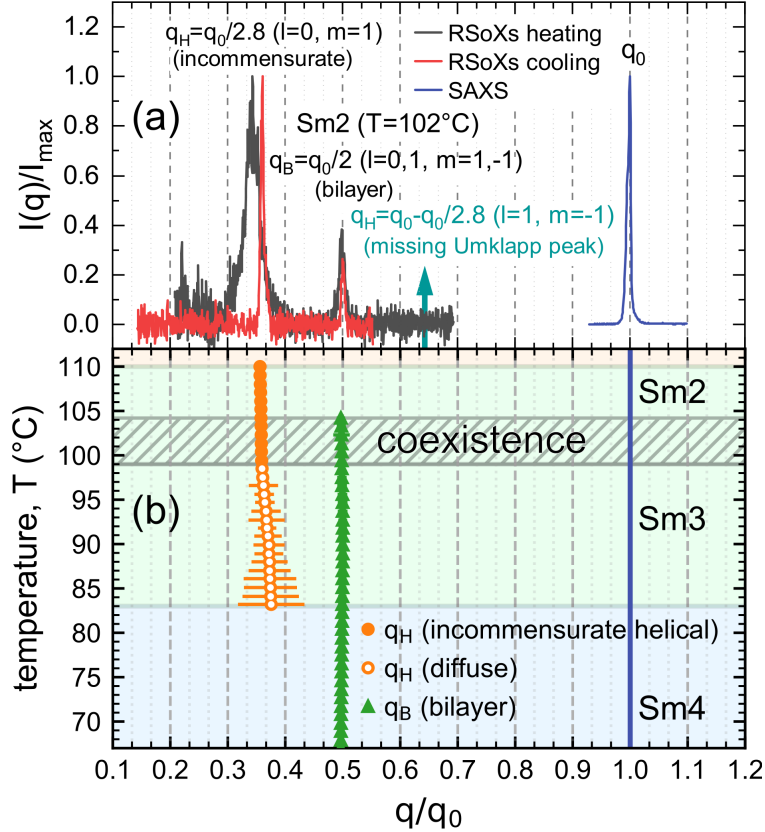


Figure 2.5: X-ray scattering from PAL30. (a) SAXS gives a peak from the smectic layer ordering at  $q = q_0$ . The RSoXS peak at  $q_H$  indicates that there is superlayer orientational ordering with periodicity  $d_H$  in the Sm2 phase. In general, superlayer orientational modulation in a smectic generates RSoXS peaks at wavevectors along the layer normal at  $q(l, m) = l(2\pi/d_0) \pm m(2\pi/d_H)$ [?]. The observation of an RSoXS reflection at  $q = q(0, 1)$  and the absence of an Umklapp peak at  $q = q(1, -1)$  in the Sm2 confirms a superlayer helix with a scattering amplitude modulation due to the smectic layering that is undetectably weak. (b) Temperature dependence of resonant scattering. The helix peak at  $q_H \approx 1/(2.8d_0)$  becomes diffuse in the Sm3 phase. Splitting of the bilayer peak at  $q_B$ , which would indicate helical precession of the bilayer structure, is not observed.

The RSoXS scattering from a single layer can be analyzed, following Levelut and Pansu, in terms of a monoclinic second-rank tensor with a principal axis tilted from and then azimuthally rotated about the layer normal [?, ?, ?]. Scattering from a stack of such layers is calculated by summing over the contributions of the individual layers at different  $z$ . Resonant scattering peaks from azimuthally periodic arrangements are found at wavevectors along  $z$ ,  $q(l, m) = l(2\pi/d_0) \pm m(2\pi/p)$ , where  $p$  is the pitch. In principle, resonant scattering should appear at all values of  $l$  (harmonics of  $q_0$ ), and at values of  $m = 0, \pm 1, \pm 2$  that depend on the superlayer structure. In an incommensurate, helical structure, like the SmC $\alpha$  phase, only the fundamental and harmonic peaks at  $q(l = 0, m = +1, +2)$  and the Umklapp peaks at  $q(l = +1, m = -1, -2)$  are found in the range  $0 < q(l, m) < q_0$ . If the resonant scatterers are confined to lie precisely on layers spaced by  $d_0$ , then the intensities of these peaks will be identical [?]. Out-of-layer molecular positional fluctuations, and, in particular, those for which there is a coupled azimuthal orientation that keeps the molecule on the helix,  $\delta\phi = (2\pi/p)\delta z$ , reduce the intensities of the resonant harmonic peak at  $2q_H$  and of the Umklapp peaks at  $q_0 \pm q_H$ , relative to that of the fundamental at  $q_H$  [?]. In our RSoXS scans of these peaks, only the fundamental is seen above the background, so that only the upper limit of the intensity ratio of the Umklapp and fundamental peaks can be estimated. From the RSoXS heating scan of Figure 2.5(a), we find  $I_U/I_F \lesssim 0.03$ , implying a very weak fractional modulation of the density of helical scatterers,  $\rho$ , due to fluctuations in the smectic layering  $\sqrt{\langle \delta\rho^2 \rangle}/\rho_0 < 0.17$ . The absence of the harmonic peaks places a similar limit on how much the density modulation of helical scatterers deviates from being purely sinusoidal.

#### 2.1.4 Optical Textures

The optical textures of planar-aligned (bookshelf) cells of PAL30 were studied using PLM. Upon cooling from the isotropic, the Sm1 phase grows in (at 175 °C) as bâtonnets, giving a smooth, focal-conic texture typical of an orthogonal fluid smectic (Figure 2.1(f),

Figure 2.6).

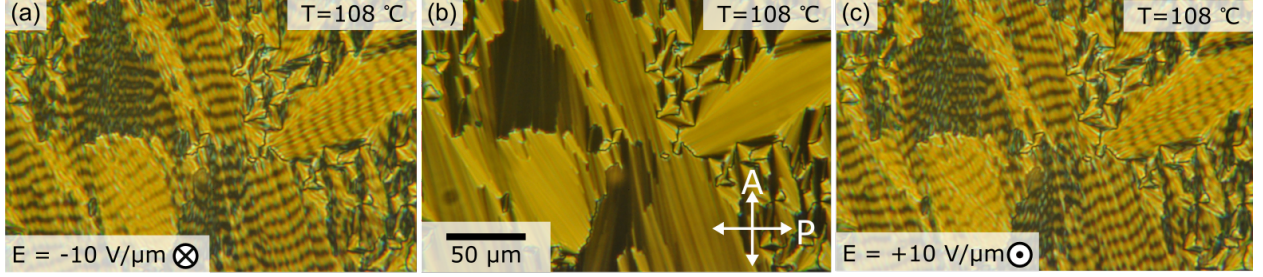


Figure 2.6: Planar aligned textures of Sm1. (a) Applied field out of the page, (b) ground state (no field), (c) applied field into the page.

However, given the large value of the estimated molecular tilt,  $\theta_{\text{xray}}$ , the Sm1 is probably a de Vries smectic. In planar-aligned cells, there is no observable field-induced change of the in-plane birefringence,  $\Delta n = n_{||} - n_{\perp}$ , in small applied electric fields (Figure 2.1(f)), or in the optic axis orientation,  $\theta_{\text{opt}}$  (Figure 2.7).

Below 115 °C, a threshold field,  $E_{\text{th}}$ , above which a first-order structural change marked by the appearance of chiral conglomerate domains occurs, becomes experimentally accessible. These domains are polar and exhibit a uniform, saturated optic axis tilt on the order of  $\theta_{\text{opt}} \approx 18^\circ$  from the layer normal, implying that the achiral, untilted Sm1 phase transforms in the field to a B2-like, homochiral  $\text{SmC}_S P_F$  state (Figure S1(c)) [?]. The field-induced left- and right-handed domains form a “tiger stripe” pattern (Figures 2.1(e,g)).

The local domain handedness in this unusual conglomerate texture is apparently locked in after the first few field cycles. This bias is due to a chiral memory effect at the surface since, as Figures 2.1(d) and 2.7 show, the sub-threshold bulk state has an achiral field response, with a linear polarization current (implying  $P \propto E$ ) and no detectable reorientation of the optical tilt.  $E_{\text{th}}$  decreases strongly on cooling as the transition to the Sm2 phase is approached, as shown in the inset of Figure 2.7.

In the lower part of the Sm1, and throughout the Sm2, Sm3 and Sm4 phases, the birefringence increases on application of an electric field, as seen in Figure 2.1(c), changing

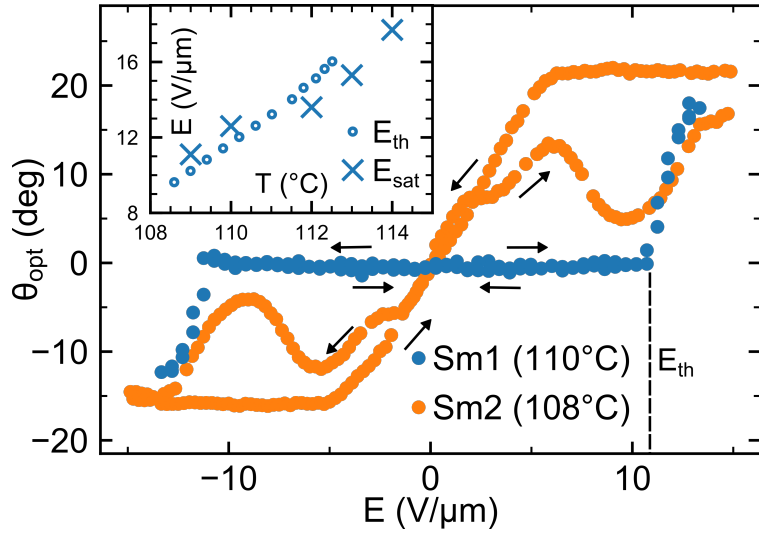


Figure 2.7: Optical tilt of PAL30 vs. applied field. The Sm1 phase shows no electrooptic response in weak fields  $E < E_{\text{th}}$ . Fields  $E > E_{\text{th}}$  induce an electroclinic tilt and result in the formation of chiral domains.  $E_{\text{th}}$ , which becomes smaller with decreasing  $T$  (inset), matches closely  $E_{\text{sat}}$ , the field at which the induced polarization saturates, extracted from Figure 2.1(d). The Sm2 phase exhibits a chiral electroclinic effect near  $E = 0$  and hysteresis in the field-induced helix unwinding to the  $\text{SmC}_\text{S}P_\text{F}$  state.

from yellow to orange. Measurements of  $\Delta n$  at  $E = 0$  and  $E = 20 \text{ V}/\mu\text{m}$  (Figures 2.1(c) and S6), show that the birefringences in the lower temperature phases with and without an applied field are of the order of  $\Delta n_{\text{on}} \sim 0.12$  and  $\Delta n_{\text{off}} \sim 0.10$ . Assuming that the field-on  $\text{SmC}_\text{S}P_\text{F}$  state (Figures 2.1(n–p) and S1) gives a uniform director orientation with the optic axis in the plane of the cell, then  $\Delta n \sim 0.12$  would correspond to the maximal birefringence  $n_3 - n_1$  of the  $\text{SmC}_\text{S}P_\text{F}$  state. Modeling the bent-core molecule as two uniaxial, birefringent rods connected with an opening angle of  $\Psi$ , and tilting this molecule from  $z$  by an angle  $\theta$ , we have calculated the birefringence of all of the states shown in Figure 2.1. If the Sm1 phase is assumed to be a de Vries SmA, with azimuthally averaged molecules distributed on a tilt cone of angle  $\theta$ , the best fit to the measured birefringence values  $\Delta n_{\text{on}}$  and  $\Delta n_{\text{off}}$  is obtained with  $\Psi = 150^\circ$  and  $\theta = 15^\circ$ . The calculated birefringence as a function of temperature is shown in Figure S6.

The transitions between the smectic phases are difficult to see when  $E = 0$  because they

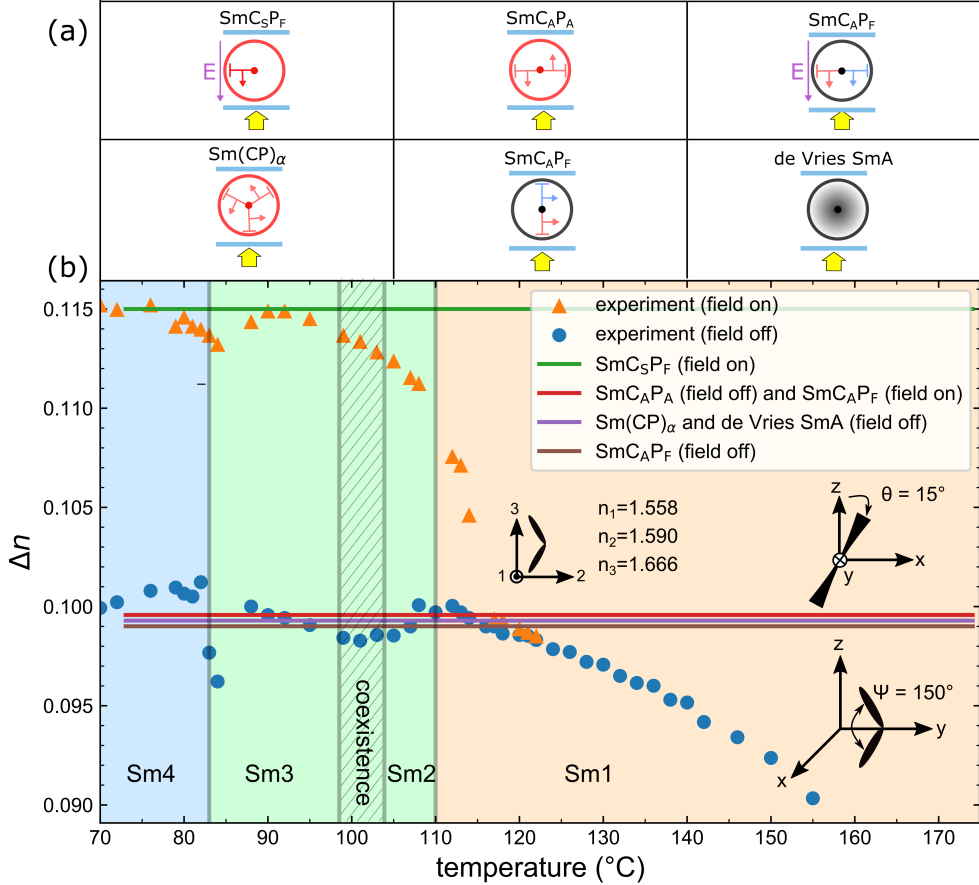


Figure 2.8: Calculated birefringence of PAL30, assuming Boulder phase assignments, shown as a function of temperature

are all orthogonal in appearance, with an optic axis along  $z$ , and have similar birefringence. At the transition from Sm1 to the Sm2 phase, however, arbitrarily small electric fields induce molecular tilt in the (Figure 2.7), leading to the formation of optically distinct, conglomerate chiral domains with opposite tilt (Figures 2.1(h–j)), again corresponding to a field-induced transition to a Sm $C_S P_F$  state. The birefringence and orthogonal appearance of the Sm2 ground state are consistent with the helical superlayer structure indicated by RSoXS.

The texture and birefringence of the Sm3 phase in the absence of field are consistent with the Sm $C_A P_A$  bilayer structure indicated by RSoXS. The field-induced conglomerate domain morphology in both the Sm2 and Sm3 phases is distinct from that of the undulating Sm1 tiger stripes, with straight domain boundaries that tend to form parallel to the layers,

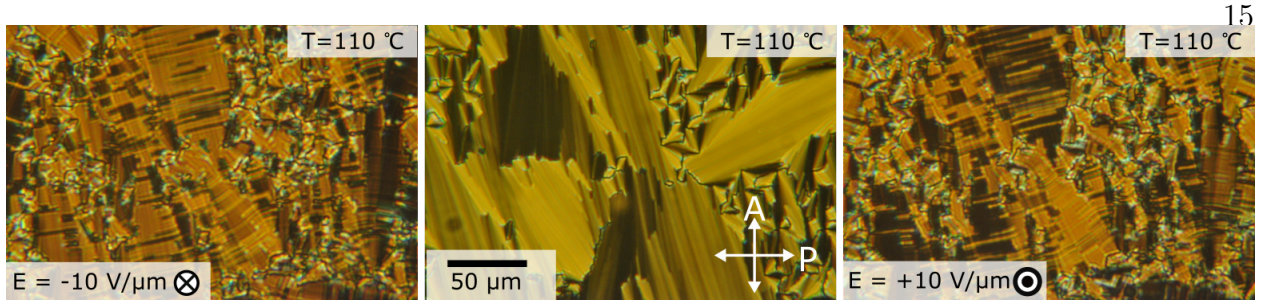


Figure 2.9: Textures of both the Sm2 ( $\text{Sm}(\text{CP})_\alpha$ ) and Sm3 ( $\text{SmC}_\text{A}\text{P}_\text{A}$ ) phases of PAL30: reminiscent of a  $\text{SmC}_\text{A}\text{P}_\text{A}$  texture.

as in an antiferroelectric calamitic being driven to a ferroelectric state [?]. The optical tilt in these domains is found to be  $\theta_{\text{opt}} \sim 18^\circ$ .

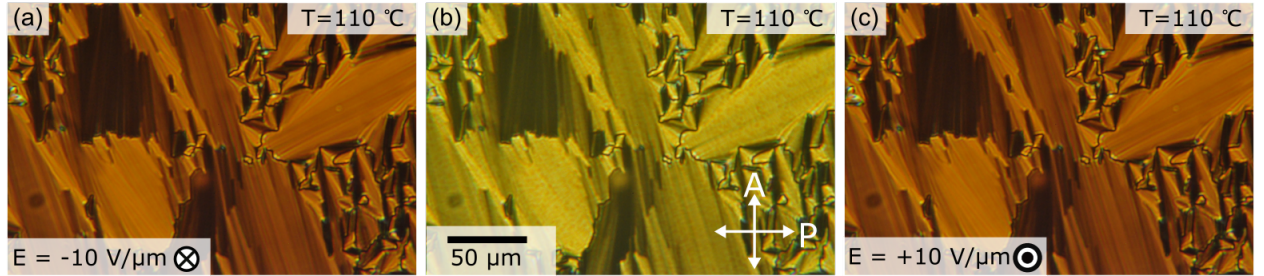


Figure 2.10: Textures of both the Sm2 ( $\text{Sm}(\text{CP})_\alpha$ ) and Sm3 ( $\text{SmC}_\text{A}\text{P}_\text{A}$ ) phases of PAL30: reminiscent of a  $\text{SmC}_\text{A}\text{P}_\text{A}$  texture.

The response to applied field changes dramatically again at the transition from Sm3 to Sm4, with no visible brush rotation or evidence of domain formation at any  $E$ .

The birefringence in the Sm4 phase increases continuously with field, saturating at a value comparable to that observed in the field-induced Sm2 and Sm3 conglomerate domains.

### 2.1.5 Polarization Current

The polarization current, measured with a triangular applied field, for the entire phase sequence is shown vs. temperature in Figures 2.1(d) [Figure 2.11](#). The polarization current will be discussed in order of cooling.

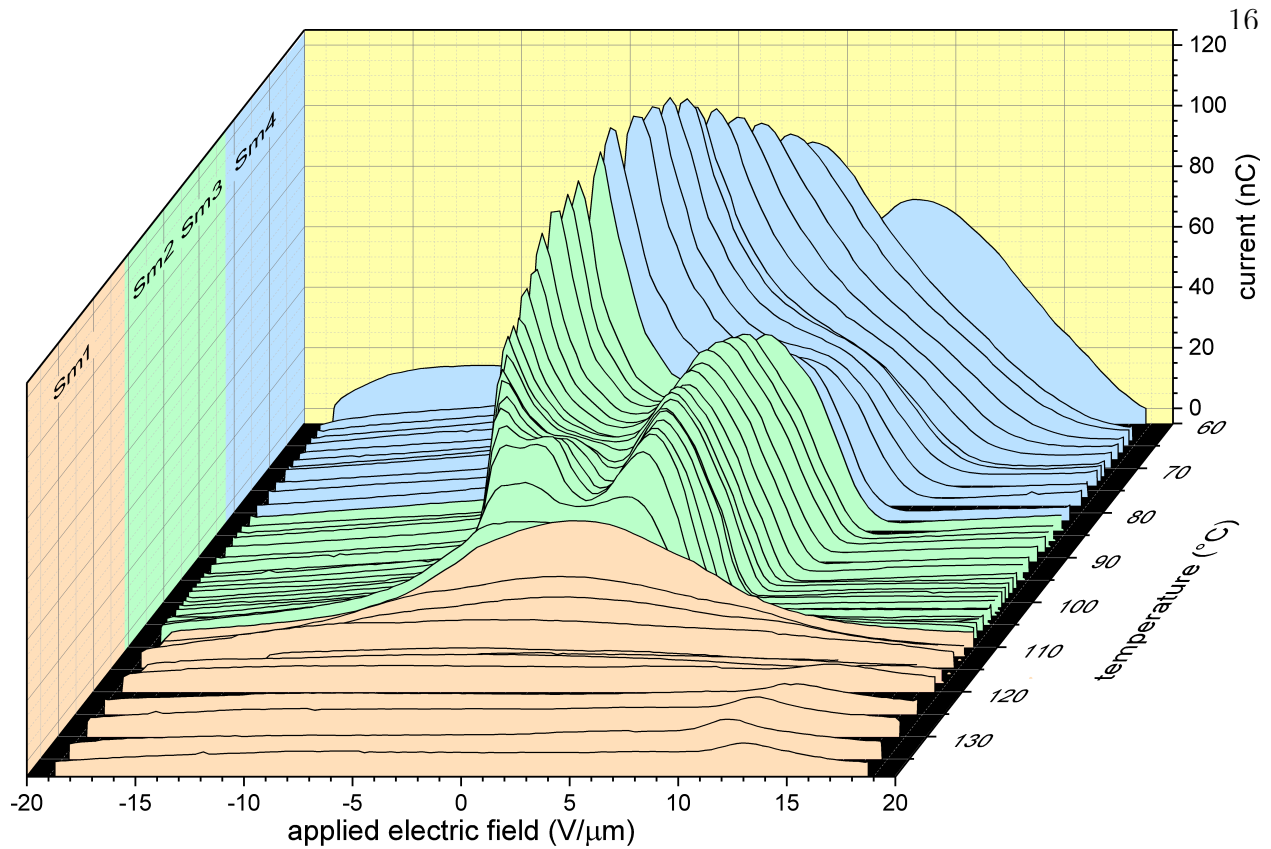


Figure 2.11: Polarization current of PAL30 shown as a function of the applied field strength.

Upon cooling from the isotropic, a single current bump centered about  $E = 0$  first appears at lower temperatures in the Sm1 phase, indicating a Langevin-type field-induced orientation of  $\mathbf{P}$ , with a linear response near  $E = 0$  and the current vanishing when  $\mathbf{P}$  becomes saturated (for  $E \geq E_{\text{sat}}$ ).

Significantly,  $E_{\text{sat}}$  is similar in magnitude to  $E_{\text{th}}$ , the threshold field required for the Sm1 transition to chirality observed optically (Figure 2.7, inset), indicating that the field first orders the Langevin system of initially azimuthally random molecular polarizations, with the Sm1 remaining in an achiral state, and that the phase becomes chiral only at higher fields, once  $\mathbf{P}$  is saturated (Figure S10).

On cooling to the Sm2 phase, the polarization bump splits into three peaks roughly centered about  $E = 0$  that evolve to two peaks on cooling through the Sm3, shown in

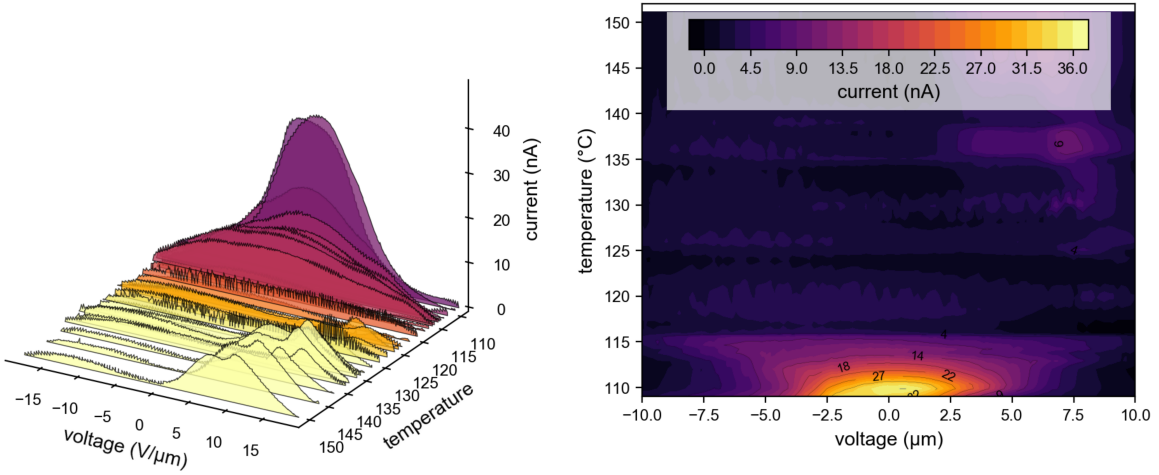


Figure 2.12: Zoomed in polarization current measurements for PAL30 in the high temperature Sm1 phase.

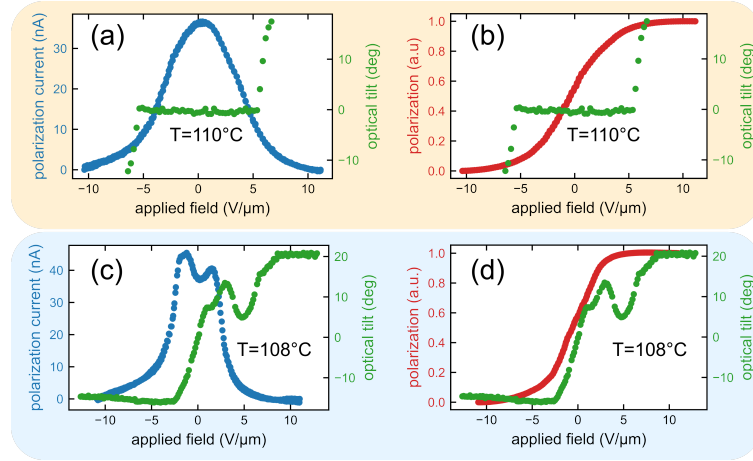


Figure 2.13: The polarization current and the optical tilt plotted as a function of applied field strength for both the Sm1 (de Vries SmA) (a,b) and the Sm2 ( $\text{Sm}(\text{CP})_\alpha$ ) (c-d). The polarization current has additionally been integrated to calculate the time-dependant net polarization. The threshold electric field ( $E_{\text{th}}$ ) required to manifest the tiger-stripes can be directly read from the green curve denoting the optical tilt (for  $T=110^\circ\text{C}$ ,  $E_{\text{th}} \approx 5 \text{ V}/\mu\text{m}$ ), and the saturation electric field where the net polarization is no longer changing ( $E_{\text{sat}}$ ) can be directly read from the red curve, which denotes the net polarization, (for  $T=110^\circ\text{C}$ ,  $E_{\text{sat}} \approx 5 \text{ V}/\mu\text{m}$ ). Both  $E_{\text{th}}$  and  $E_{\text{sat}}$  are plotted in as the inset of Figure 2.7.

Figure 2.14.

PAL30 thus transforms on cooling from the non-polar Langevin ground state of the

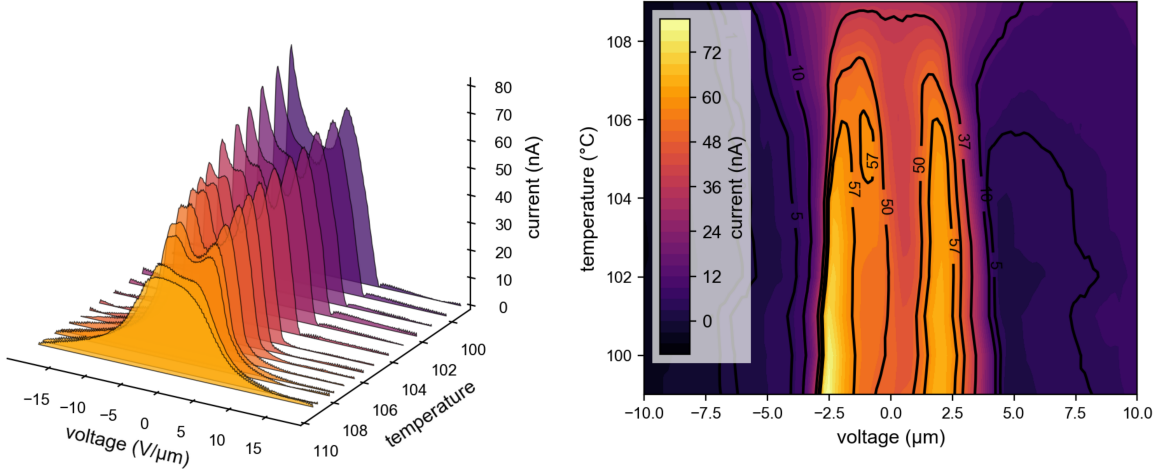


Figure 2.14: Polarization current of sm2 of PAL30 plotted against applied voltage

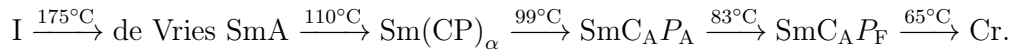
Sm1, where  $P = 0$  is enforced by entropy, to energetically stabilized ground states in which the spatial average of  $\mathbf{P}(\mathbf{r})$  in the absence of applied field is also zero: the incommensurate helical winding of the polarization in the Sm2, and the antiferroelectric bilayer structure in the Sm3.

At the transition to the Sm4, a single current peak dominates, characteristic of the block polarization switching of a ferroelectric ground state that is surface-stabilized with  $\mathbf{P}$  parallel to the cell plates at  $E = 0$ , such as occurs in the orthorhombic  $\text{SmAP}_\text{F}$  phase [?].

The absence of brush rotation during the field-induced reorientation of the polarization in Sm4 is consistent with achiral  $\text{SmC}_\text{A}\text{P}_\text{F}$  superlayer organization.

## 2.2 Results and Discussion

In summary, X-ray and optical experiments show that PAL30, an achiral, bent-core mesogen, forms smectic liquid crystal phases with the molecules substantially tilted from the layer normal, with phase sequence:



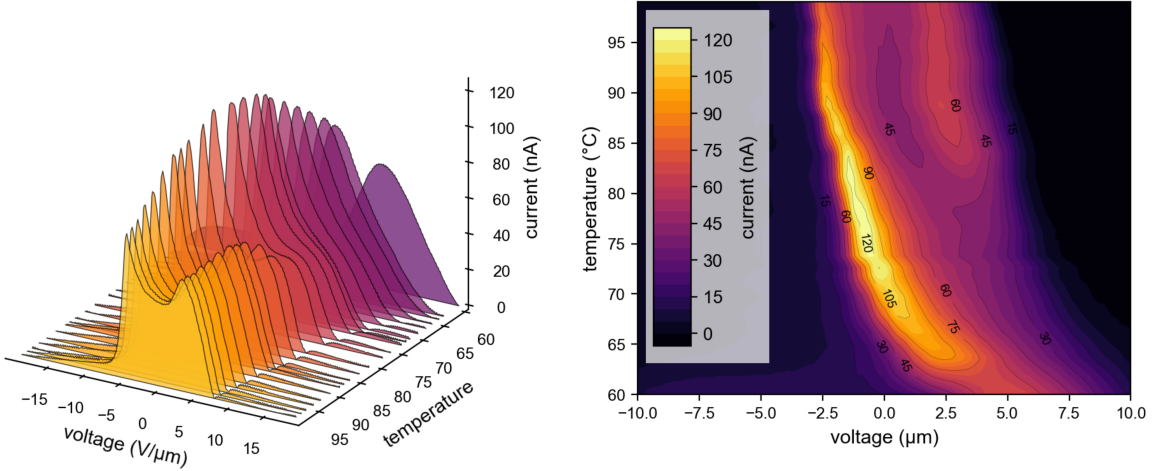


Figure 2.15: Polarization current measurements for PAL30 in the high temperature Sm1 phase.

The highest temperature phase exhibits short-ranged ordering of the tilt azimuth that is decoupled from the molecular polarization, forming a uniaxial, non-polar, achiral de Vries smectic A. An applied electric field of increasing magnitude continuously aligns the initially random polarization and the phase acquires orthorhombic symmetry. The field eventually saturates the polarization orientation, inducing a transition to a tilted, chiral, ferroelectric smectic state.

Upon cooling, a novel chiral, ferroelectric phase which we call the  $\text{Sm}(\text{CP})_\alpha$  appears. This phase is similar to the  $\text{SmC}_\alpha$  phase of chiral, rod-shaped molecules [?, ?, ?, ?], but with the chirality appearing here as a broken symmetry. A periodic azimuthal precession of the director about the layer normal that is incommensurate with the smectic layering is confirmed by the presence of Bragg reflection peaks in carbon-edge resonant soft X-ray scattering. The absence of the corresponding resonant Umklapp peak unambiguously identifies this structure as a helical modulation of the orientational ordering in which molecules exhibit substantial coupled rotational/positional out-of-layer fluctuations, forming a twist-bend-like helix.

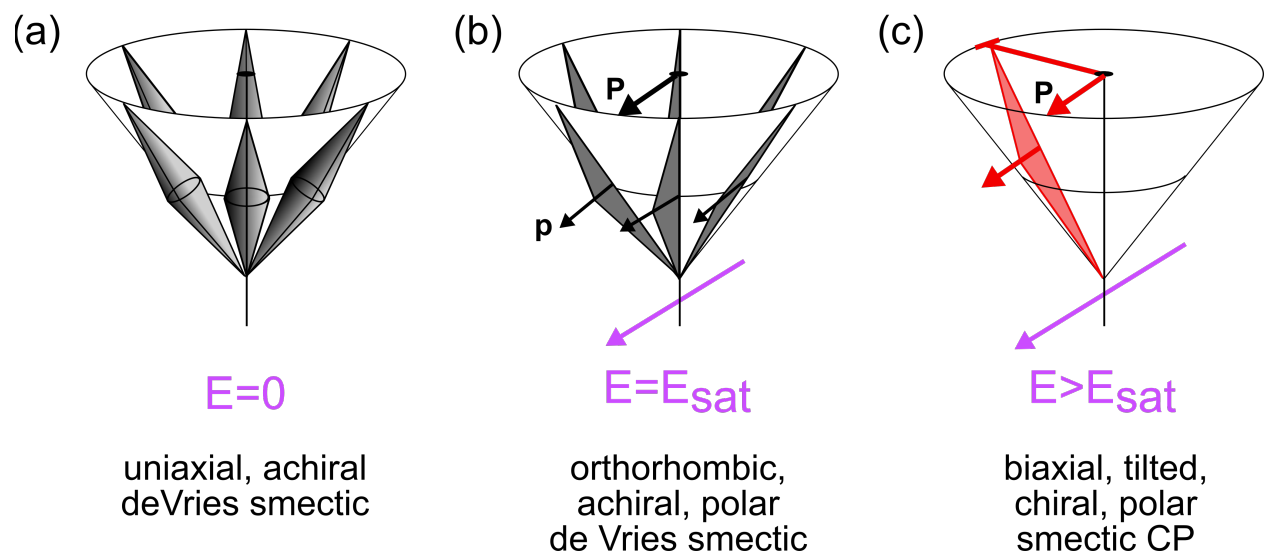


Figure 2.16: Evolution of de Vries SmA bent-core phase under the application of a field

## Chapter 3

### Future Work: Structure-Property in the PAL30 Homologous Series of Molecules

Now that the existance of the  $\text{Sm}(\text{CP})_\alpha$  and  $\text{SmC}_\text{A}\text{P}_\text{A}$  phase have been put on a firm footing, we can extend this study to a broad category of molecules that share the same core, but have variations in the tail length. Our previous study focussed on PAL30, with a tail length of  $n=14$  carbons. Inspired by previous studies by the Dublin group[?, ?, ?], where the  $n_{16}$  and  $n_{18}$  compounds were studied and a helical phase was tentatively determined based on periodicities of around  $5n$  seen in atomic force microscopy images. This is a test. With the ability to directly probe the periodicity of these compounds with carbon K-edge resonant X-ray, we have the ability to provide direct evidence for helical phases in these molecules. The high-resolution provided by RSoXS additionally allows for a rich study of structure-property relationships, where the nature of the helical phase can be connected to the tail-length.

Interest in the PAL30 series of molecules is not confined to the discovery of helicity. The additional discovery of a bent-core de Vries like phase is also a motivating interest for study of this series.

This chapter is organized under discussion of these two phases. First the helical, smectic  $\text{Sm}(\text{CP})_\alpha$  is presented and discussed for the  $n_{12}$ ,  $n_{14}$ , and  $n_{16}$  molecules. Then the bent-core de Vries phase is presented and discussed for this series.

### 3.1 The $\text{Sm}(\text{CP})_\alpha$ Phase: Smectic Chirality Beyond the B2 Phase

### 3.2 The bent-core de Vries phase

The evidence for a bent-core de Vries phase in PAL30 will be briefly reviewed. It is worth noting that the question of “what is a de Vries phase” is not settled, even for the simpler phases of rod-shaped molecules, see Jan Lagerwall’s thesis[?] for an excellent history and discussion of de Vries phases in the calamitic paradigm. For the purposes of this thesis, we take the broadest view of a de Vries: it is a tilted phase with no long-range order present in the tilt order parameter.

Even this broad definition is not free from ambiguity— what entails long-range order, and does it matter how the escape from long-range order is achieved? We will also see in this Chapter that the de Vries phase can be suppressed quite easily by a strong-alignment layer.

To satisfy our definition, we must prove two things about the phase under investigation to say it is a de Vries bent-core phase. First, it must be tilted. Second, it must have no long-range order present. Both of these facts are very difficult to establish in a positive manner, as there is no ‘smoking-gun’ evidence for either.

We claim that PAL30 is tilted for the following reasons: the smectic layer spacing is significantly less than the extended molecular length; the lower temperature phases are proven to be chiral (therefore tilted), and there is no observed smectic layer-contraction observed on cooling, which would be expected for an orthogonal → tilted phase transition; and there is no measured change in the birefringence which would be predicted from an orthogonal phase to the helical  $\text{Sm}(\text{CP})_\alpha$  (confirmed from RSoXS). Though individually, none of these facts are conclusive evidence for tilt, all of them in aggregate suggest that the highest temperature smectic phase of PAL30 is tilted. To see that there is no long-range order in the tilt order parameter, we can look at the textures of this phase and observe that they look orthogonal–

they have the clean lines of a focal conic SmA phase. This is necessary but not sufficient, as other phases – such as the  $\text{SmC}_\text{A}P_\text{A}$  phase – can also appear to be orthogonal, yet have a definite anti-clinic long range order. This anti-clinic order (and other, more exotic long helical ordering of the tilt order parameter) would however, show up in resonant x-ray scattering. The fact that the resonant x-ray scattering shown in ?? reveals zero periodic structure for PAL30 confirms that the tilt order in the Sm1 phase has no long-range order.

The actual way that this long-range order is escaped is still ambiguous. The simplest model, where the molecules are rotating freely around a cone whose opening angle is set by the molecular tilt seems unlikely from simple enthalpic space-filling arguments which would seem to exclude a model where neighboring molecules can be pointing in completely opposite directions with no energy cost. On the surface, this seems to be false, but close observation of the c-director fluctuations that occur in freely-suspended-films shows that at the molecular level the c-director can easily be fluctuating with  $\pi$ -rotations measured against neighboring molecules, so we cannot rule out this type of behaviour purely on enthalpic concerns. This is fluid-like model, where the molecules are actively rotating with no regard for their neighbors space.

By including these enthalpic considerations we can build model where short-range order persists, but the size of these ordered domains is small, and they are randomly distributed such that an ensemble average of the tilt is zero. This is more of a disordered-crystal model, where short-range order persists, but is distributed in such a way that the macroscopic order parameter is still zero – much like the example of a cooled Ising model developing local ferroelectric ordering of spins, even though the total magnetization remains zero.

Regardless of how this long-range tilt order is broken, because these are polar molecules, we also have to consider the polar-ordering present in any phase. The way that the polar and tilt interact in the high-temperature de Vries SmA of PAL30 is unique to bent-cores.

The polarization current has been integrated to give the net polarization, which is a direct measure of the ensemble average of the molecular polar orientation with an applied

need  
to find  
de  
gennes/  
argu-  
ment  
for  
this

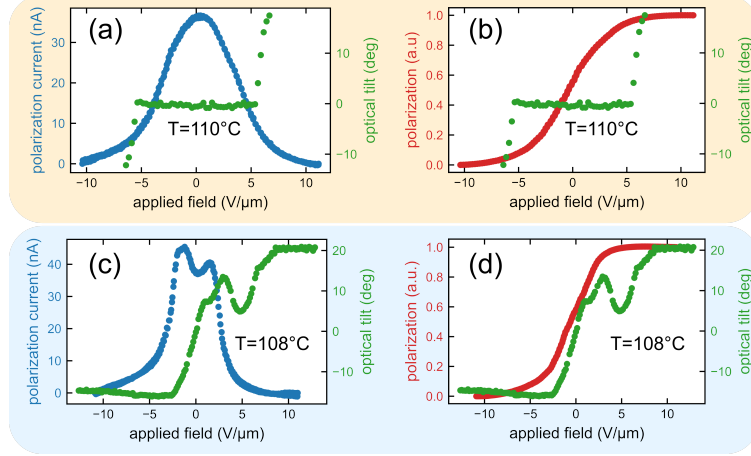


Figure 3.1: The polarization current and the optical tilt plotted as a function of applied field strength for both the Sm1 (de Vries SmA) (a,b) and the Sm2 ( $\text{Sm}(\text{CP})_\alpha$ ) (c-d). The polarization current has additionally been integrated to calculate the time-dependant net polarization. The threshold electric field ( $E_{\text{th}}$ ) required to manifest the tiger-stripes can be directly read from the green curve denoting the optical tilt (for  $T=110^\circ\text{C}$ ,  $E_{\text{th}} \approx 5 \text{ V}/\mu\text{m}$ ), and the saturation electric field where the net polarization is no longer changing ( $E_{\text{sat}}$ ) can be directly read from the red curve, which denotes the net polarization, (for  $T=110^\circ\text{C}$ ,  $E_{\text{sat}} \approx 5 \text{ V}/\mu\text{m}$ ). Both  $E_{\text{th}}$  and  $E_{\text{sat}}$  are plotted in as the inset of Figure 2.7.

electric field. The optical tilt measurements were done by analyzing the contrast between adjacent stripes. In the ground state, where there is no long-range order present in tilt, the contrast is zero. At a field whose strength is over some threshold value ( $E_{\text{th}}$ ), the state transitions into a tilted (therefore chiral) state. The handedness of the domain sets the tilt direction. This tilt can be directly measured as it is proportional to the contrast between different handed domains:

$$\text{contrast} \propto \sin(4\theta) \quad (3.1)$$

Barring pathological examples, any alignment, orientation, or movement of the molecular long axis will show up as the observable separation of the texture into chiral domains.

With some unique exceptions[?] most bent-core systems have the tilt and polarity strongly coupled: where one moves, the other follows. Through symmetry, this can be expressed as the condition that rotations around the molecular long axis are forbidden: to transition to different states, the molecule must rotate around the smectic layer normal,

small  
figure  
show-  
ing  
this

check  
this

cite  
michi

confined to the tilt-cone. Figure 3.1 clearly shows that for the Sm1 phase of PAL30, this is no longer the case. The movement of the polar director is completely decoupled from the movement of the c-director, which can only occur if the PAL30 molecules are rotating around the long axis, allowing their polarization to change while the optical tilt stays fixed. It is only after the polarization saturates and is completely aligned before there is any detectable movement of the tilt-director. The previous examples of this occurring in bent-cores required pulse-engineering the applied voltage, where a very large, fast voltage needed to be applied to see rotations around the long axis of the molecule. PAL30 is the first molecule where the polar and tilt order are decoupled enough to allow these long-axis rotations naturally.

This decoupling results in an important distinction because, unlike their calamitic cousins, these bent-core molecules are not inherently chiral. They are only develop chirality once they pack into phases. they require tilt and smectic ordering before the mirror-symmetry breaking required for chirality is achieved. They also require that the tilt and polar order are strongly coupled–free rotations around the long-axis result in a return of mirror-symmetry and the chirality of the phase is lost. In contrast to the calamitics, who merely have to ‘discover’ their own inherent chirality once a field is applied (for instance, in the electroclinic effect), the bent-cores must spontaneously create their own. This is not a new discovery, the B2 phases[?] have long been known to develop spontaneous chirality on cooling from an achiral phase. This is however the first discovery of field-activated chirality in a bent-core system, where chirality is induced at a certain voltage, but then returns to an achiral ground state when the voltage is removed.

The bent-core de Vries phase we discovered in PAL30 has three defining characteristics: it is tilted; it has no long-range tilt-order present, and the polarity and tilt are decoupled.

One potential approach to modelling this phase is the Landau-de Gennes model put forth by Eremin et al.[?] where they discovered an electro-clinic analog in a hockey-stick compound. Broadly, their model describes an orthogonal bent-core phase where the polar director is free to move. On application of an electric-field, the polarization of the molecules

small  
inline  
figure  
of this

get  
and  
show  
the  
molecule

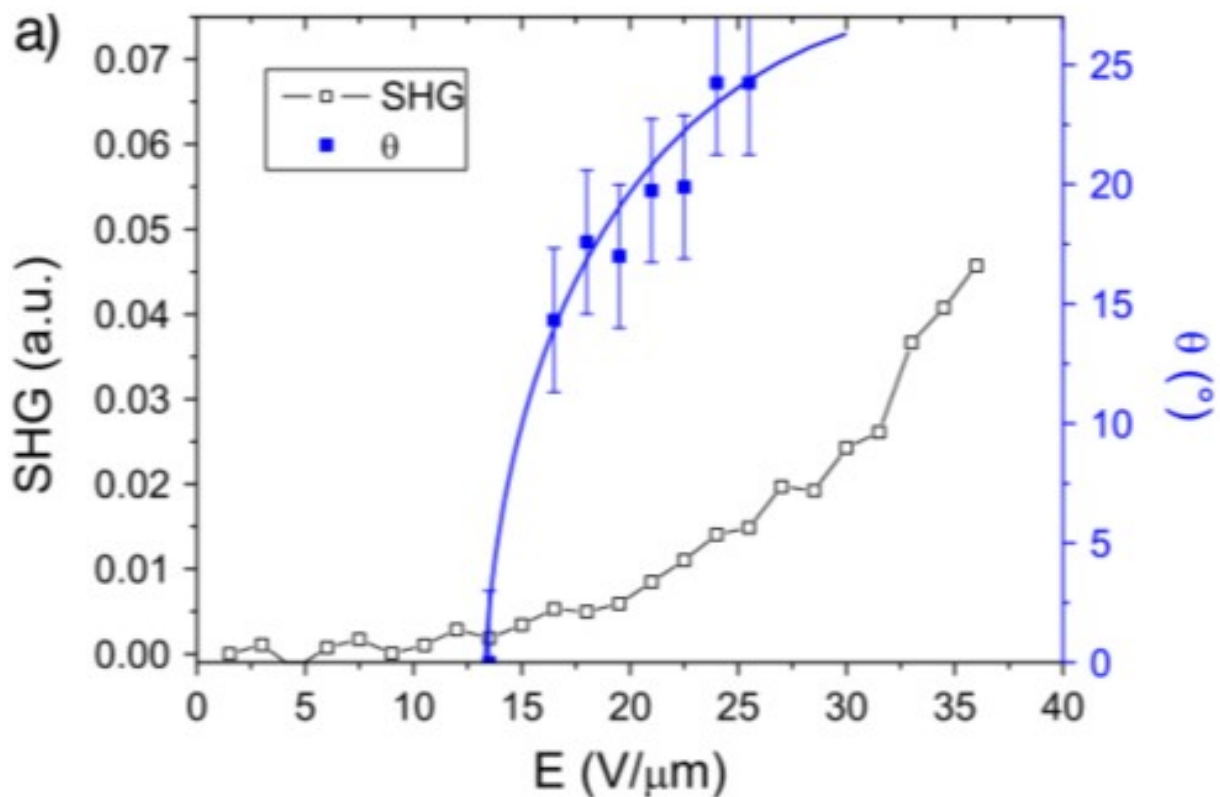


Figure 3.2: Experimental data for ‘hockey-stick’ compound studied by Eremin et al.[?] Note, the threshold for optical tilt. The lines guide the eye.

orients. An enthalpic phase transition is then driven by excluded-volume interactions, where the molecules can pack more efficiently by tilting.

This interaction is described by the following Landau-de Gennes free energy:

$$f(P, \theta, T, E) = \overbrace{(a_0(T - T_\theta)\theta^2 + b\theta^4 + c\theta^6)}^{f_\theta} + \underbrace{(\alpha_0(T - T_P)P^2 + \beta P^4 + \gamma P^6 - PE)}_{f_P} + \underbrace{(-\Gamma(P\theta)^2)}_{f_{\theta P}} \quad (3.2)$$

Though this model was originally formulated to describe the transition from an orthogonal phase to a tilted one, we can adapt it to our bent-core de Vries phase by changing the interpretation of  $\theta$  from the molecular tilt to the optical tilt.

Though this model successfully captures the overall nature of the electrically-driven onset of chirality in the bent-core de Vries phase, where the molecules first orient their polar directors to the field, and on the achievement of total polar alignment, an optical tilt develops, it leaves much to be desired. Because this model does not demand details of the microscopic interactions that lead to the observed transition, there is an abundance of fitting parameters that will lead to overfitting and the model loses most of its predictive power.

Because of this, efforts must be undertaken to develop a microscopic model of this de Vries phase.

### 3.2.0.1 The Beginnings of a Microscopic Model for the Bent-Core de Vries

Though the full development of this theory is beyond the scope of this thesis, I will outline the steps that must be taken.

First, the decoupling present between the polar and tilt order in the bent-core de Vries phase has to be experimentally quantified. This decoupling is realized when the molecule can rotate freely around the long axis, which can be described by a single angle,  $\beta$ . The other switching mode, common to conventional bent-cores, is described by a rotation around the tilt

check  
this  
with  
ed

cone, described by an angle  $\theta$ .

### 3.2.1 Textures of bent-code de Vries phase

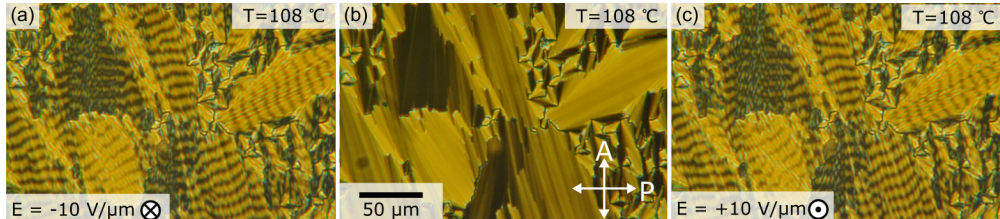


Figure 3.3:

### 3.2.2 Electro-optics of bent-core de Vries phase

text text

text

### 3.2.3 X-ray analysis of bent-core de Vries phase

## 3.3 Discussion for the bent-core de Vries phase

## 3.4 Alignment-Induced Phase Transitions

It is easy to ignore that when experimentalists perform phase characterization of liquid crystals, we are not only characterizing the phase in terms of the usual statistical mechanic variables of pressure and temperature, we also must include the variable of how this material was confined. An example of this is the suppression of the long-range helix in the SmC\* anti-ferro phase in thin cells. And for the majority of liquid crystal/soft matter systems, the conditions of confinement do not impact the bulk phase that dramatically, and we are right to ignore it.

include  
math  
sec-  
tion  
show-  
ing  
the ro-  
tation  
of this  
angle

using  
michi's  
model,  
dis-  
cuss  
how  
we can  
quan-  
tify

which  
mode  
of  
switch-  
ing we  
are in

cite  
noel's  
flc  
stuff

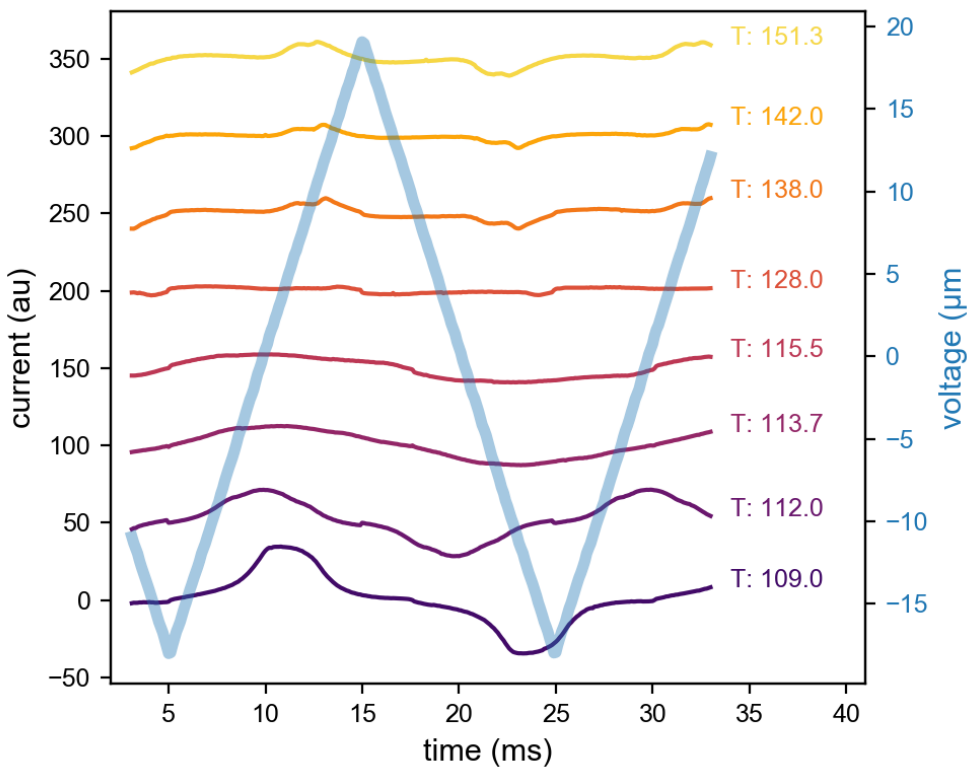


Figure 3.4:

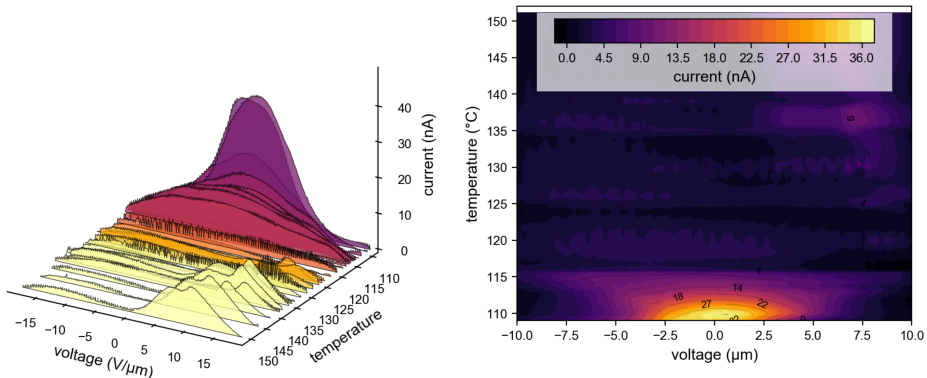


Figure 3.5:

However, our investigation of the homologous series of molecules related to PAL30 have revealed that the confinement conditions cannot be ignored for this series of molecules. ?? shows the same material, **n-16** in two different cells. One is an LC Vision cell, one is an Instec cell. .

need  
to find  
out  
what

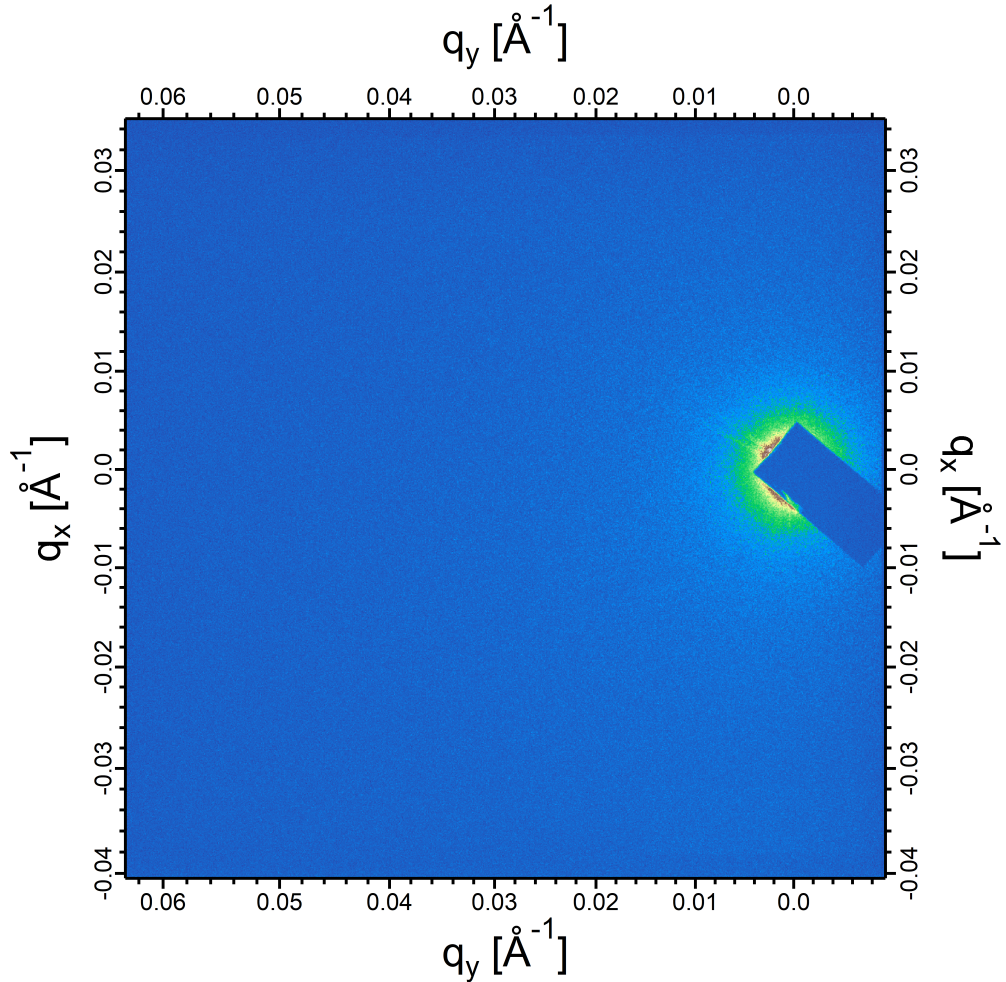


Figure 3.6:

The behaviour of the same material in these different cells is so different as to be a different phase. This observation goes a long way to explain why the original phase classification of PAL30 was so contentious- it could be that the Dublin group was actually observing a different phase from our observations in Boulder.

Though we are currently limited in our ability to compare the behaviour of these materials in different cells due to a dearth of available material, we can compare the electro-optic behaviour at different temperatures.

**n-16** begins switching at similiar temperatures on cooling from the isotropic phase, shown in [Figure 3.9](#). In LC vision cells (which were used to characterize the PAL30 compound),

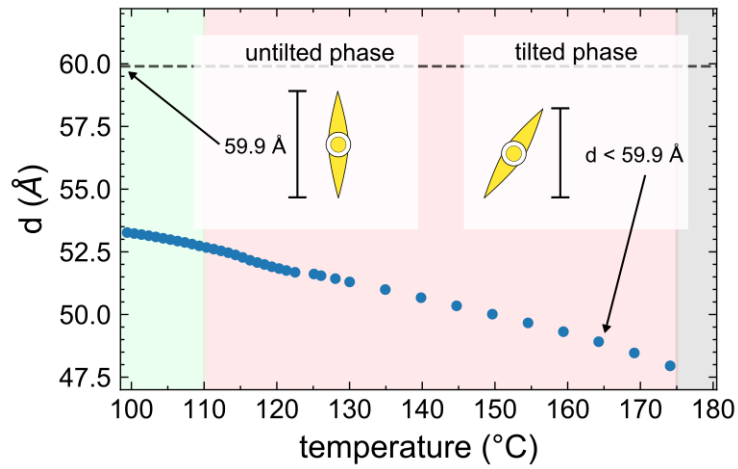


Figure 3.7:

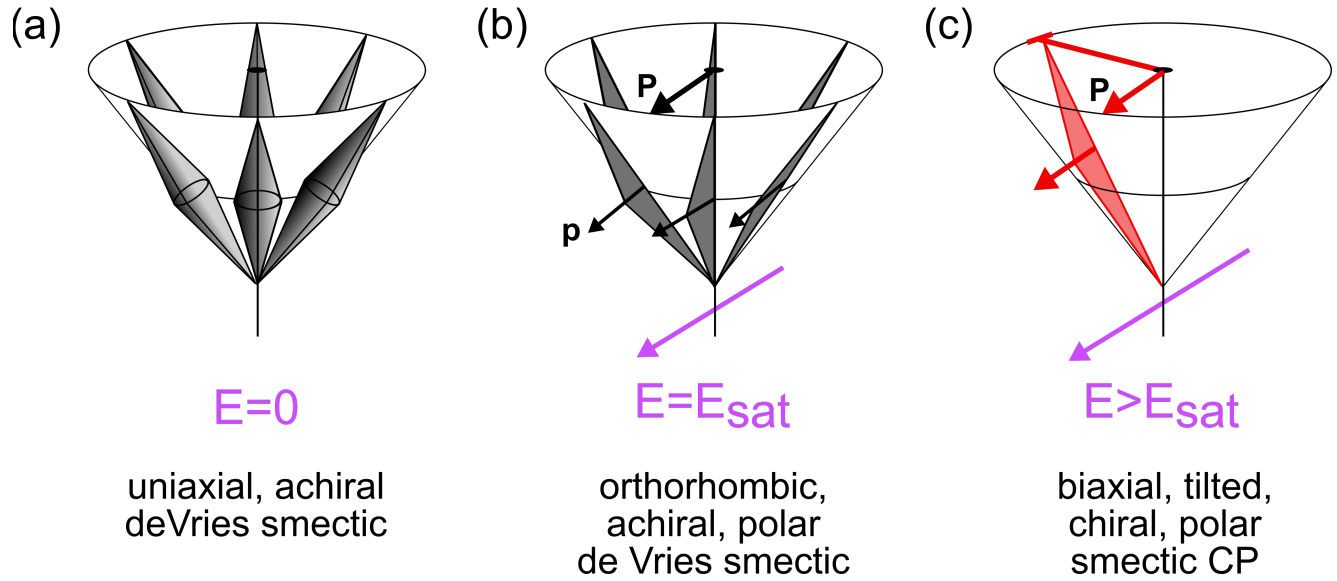


Figure 3.8:

the response to an applied electric field manifests as the familiar tiger stripes seen in PAL30 (Figure 3.9 (a-c)), with a subtle difference: while the tiger stripes seen in PAL30 were parallel to the smectic layers *on average*, they were wavy. The tiger-stripes seen in **n-16** are straight, indicating that they are rigidly bound to the smectic layers. The implications of this are not understood.

In the Instec cells, the response to an applied electric field manifest as a barely distinguishable change in contrast in large block-like regions (Figure 3.9(d-f)). However, these phases look broadly similar— an orthogonal-looking ground state that switches into some chiral phase. It is only on further cooling that the texture undergo a dramatic divergence.

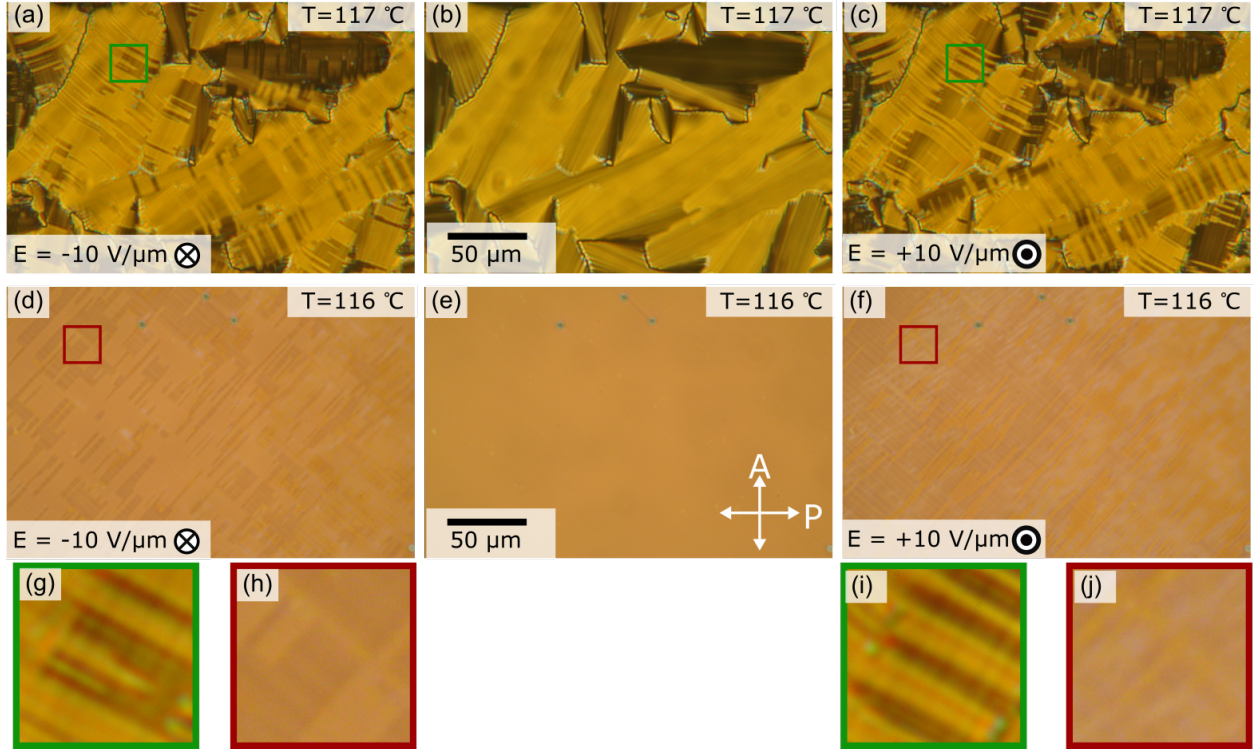


Figure 3.9: Planar textures of **n-16** at approximately 116 °C in an LC vision cell (a-c) and an Instec cell (d-f) viewed under cross polarizers. Both cells use a polyimide anti-parallel alignment layer. The LC vision cell has clear focal conics, while the Instec cell is entirely aligned. Both textures manifest chirality, seen as the distinct difference between the textures with a negative or positive out-of-plane electric field applied. The contrast between handed domains shows up clearly in the LC vision cells (compare (g) and (i)) while the contrast in the Instec cells is barely distinguishable.

Cooling to 110 °C gives a familiar  $\text{SmC}_A P_A$  like texture in the LC vision cells that looks identical to PAL30— an orthogonal like phase that switches into a clearly chiral phase, with contrast between domains of alternating chirality (Figure 3.10 (a-c)). However, the Instec cell appears to not be chiral— the positive and negative applied field result in a texture that

appears broadly identical, indicating a mirror symmetry in the phase that precludes chirality ([Figure 3.10](#) (d-f)). Instead, the birefringence increases in broad stripes that are parallel to the smectic layers. One possible explanation is that the alignment of the bottom-plate and top-plate of the cell aligned at opposite positions on the tilt-cone. This would give a texture that could appear orthogonal, even when the polarization has been universally aligned to an external field. This is not unheard of, and one way to rule this out would be to prepare a cell with an alignment layer on only one of the plates of the cell. The other possible explanation is that the dramatic alignment caused by the Instec cell, alongwith the unique decoupling of polarity and tilt seen in these molecules, are interacting in an unforeseen way.

Further cooling to 100 °C gives a unique texture in both the LC Vision cell, and the Instec cell, see [??](#). While the PAL30 textures in this phase had regular stiations of contrast present when an external field was applied, they did not manifest the riot of colour present in the **n-16** textures, where bands of different birefringences appear overlaid bands of contrast [??\(a-c\)](#). The cause of this is currently unknown. It is also worth noting that this state appears to be long-lived, as inspection of the texture that was previously exposed to an electric field in [?? \(b\)](#), still manifest faint striations, indicating that it has not fully relaxed to an achiral ground-state.

This stands in contrast to the Instec cell, whose response under an applied electric field has actually decreases. The bands of birefringence clearly visible at 110 °C in [Figure 3.10](#) (d,f) have faded. However, the dark bands that form orthogonal to the layers (much like those caused by undulating layers in a SmA focal conic) which were only faintly visible at 110 °C in [Figure 3.10](#) (d,f) are now more pronounced.

On further cooling, the textures of both cells converge to familiar  $\text{SmC}_\text{A}P_\text{F}$  switching, where the entire cell has an increase in birefringence under an applied electric field.

Solving this mystery will go a long way to advancing our understanding of how chirality develops and manifest in these soft-matter systems. We have a phase with a known chiral bulk-state (see the resonant x-ray scattering of **n-16** at 110 °C) that, in some cells (LC

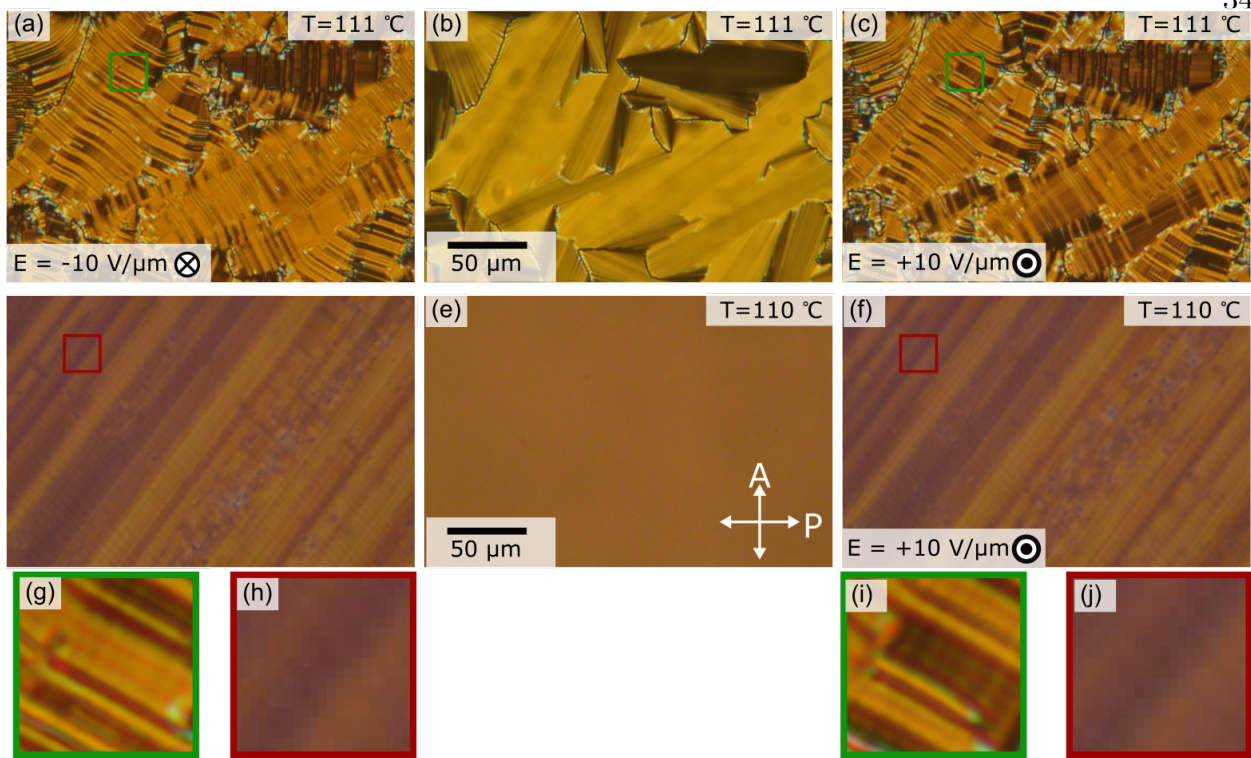


Figure 3.10: Planar textures of **n-16** at approximately 110 °C in an LC vision cell (a-c) and an Instec cell (d-f) viewed under cross polarizers. Both cells use a polyimide anti-parallel alignment layer. The LC vision cell has clear focal conics, while the Instec cell is entirely aligned. Both textures manifest chirality, seen as the distinct difference between the textures with a negative or positive out-of-plane electric field applied. The contrast between handed domains shows up clearly in the LC vision cells (compare (g) and (i)) while the contrast in the Instec cells is barely distinguishable.

vision), shows its chiral nature, but in others (Instec), this chirality seems to be suppressed. The more conventional explanation, that this is still the same chiral Sm(CP) $_{\alpha}$  phase which appears to be achiral because of some fluke in the alignment would need to first be ruled out.

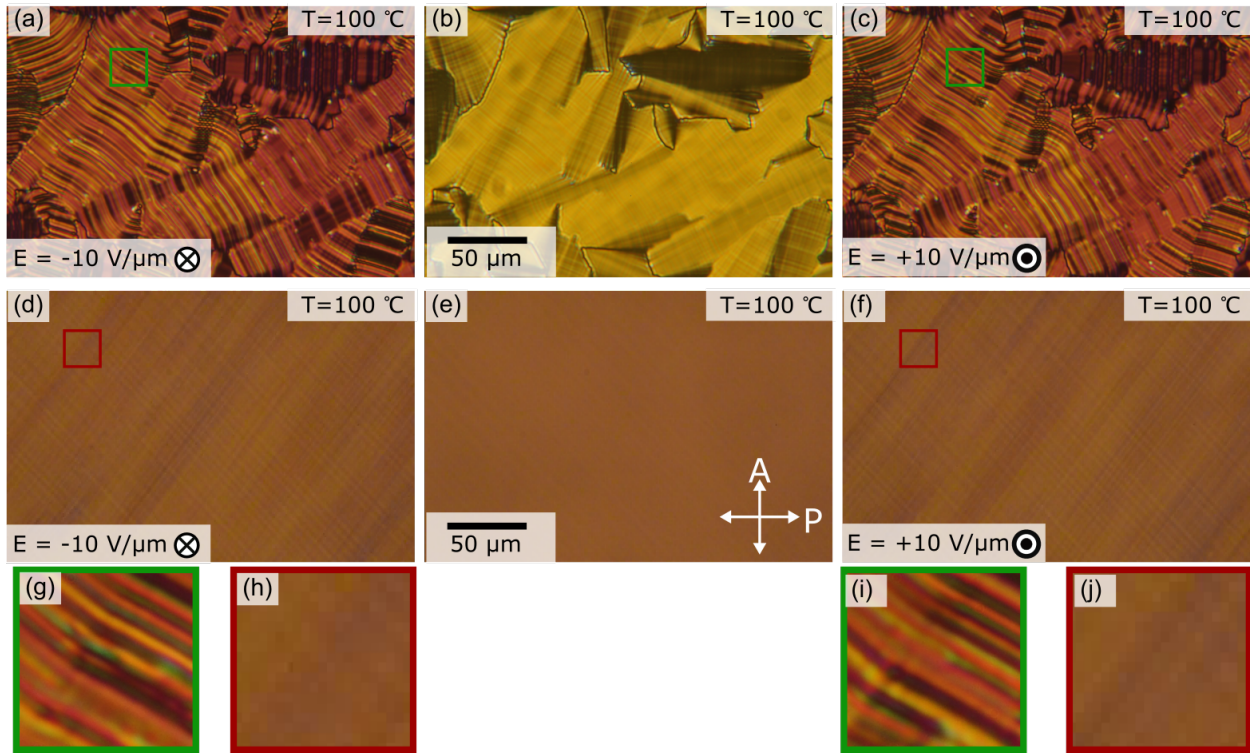


Figure 3.11: Planar textures of **n-16** at approximately 100 °C in an LC vision cell (a-c) and an Instec cell (d-f) viewed under cross polarizers. Both cells use a polyimide anti-parallel alignment layer. The LC vision cell has clear focal conics, while the Instec cell is entirely aligned. Both textures manifest chirality, seen as the distinct difference between the textures with a negative or positive out-of-plane electric field applied. The contrast between handed domains shows up clearly in the LC vision cells (compare (g) and (i)) while the contrast in the Instec cells is barely distinguishable.

## Chapter 4

### Metrology Applications of Fluid Crystals

#### 4.1 Experimental Design

We created freely-suspended smectic films with racetrack geometry, as shown in Fig. 4.1, using 8CB (*4-n*-octylcyanobiphenyl), a fluid smectic A liquid crystal at room temperature that can be drawn into molecularly thin films freely suspended in air [?, ?, ?]. A mechanical drawing of the film holder is in the Supplemental Information.

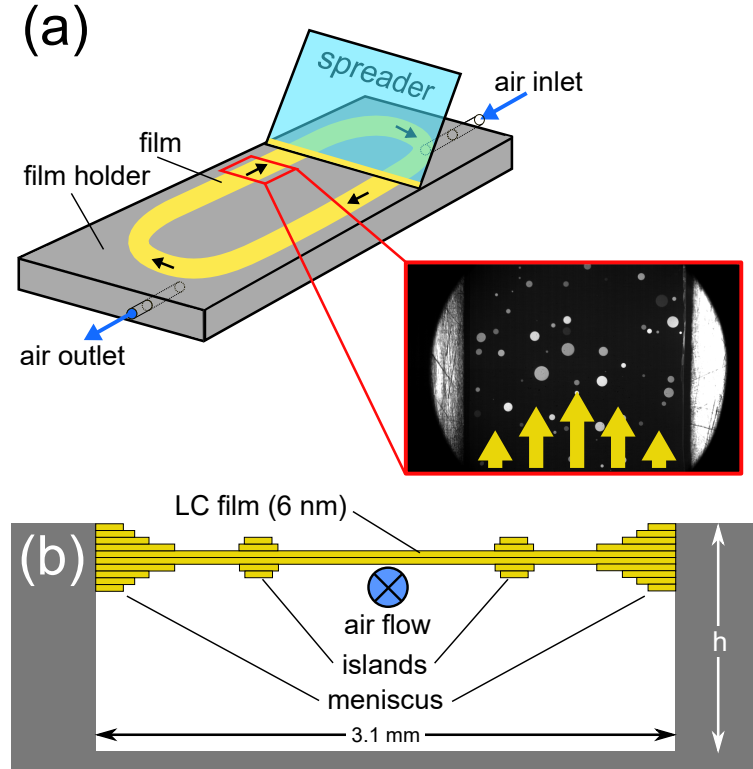


Figure 4.1: Smectic film flow meter geometry. (a) A stainless steel film holder ( $45.2\text{ mm} \times 34.8\text{ mm} \times 7.6\text{ mm}$ ) has a  $w = 3.1\text{ mm}$ -wide channel in the form of a racetrack cut to a depth  $h = 3.7\text{ mm}$ . At viewing ports centered along each ‘arm’, the channel is cut all the way through the film holder (a depth of  $7.6\text{ mm}$ ). Gas is coupled into and out of the system by means of co-linear,  $2\text{ mm}$ -diameter holes at the ends of the film holder. Smectic films are created by coating the bottom of a glass coverslip (the spreader) with liquid crystal material and drawing it across the top opening of the channel. The film is shielded from random air currents from above by a sealed cover (not shown). The photomicrograph shows typical islands (localized regions with more layers than the background film) used to track flow of the film in one of the viewing regions of the racetrack. (b) Schematic cross-section of a smectic film suspended across the channel (not to scale). The film comprises an integer number of smectic layers and can be as thin as two molecules ( $\sim 6\text{ nm}$ ). In general, a meniscus forms where the film contacts the edges of the channel.

Freely-suspended films are ideal flow sensors for several reasons. Because they are so

thin, they extract very little energy from the gas jet being measured. A comparison of the effective areal densities in our system assuming mass densities  $\rho_{LC} = 1.008 \times 10^3 \text{ kg/m}^3$  and  $\rho_{air} = 1.225 \text{ kg/m}^3$ , and thicknesses 6 nm and 1 cm of the LC film and of the layer of air in the channel respectively, shows that the mass per unit area of the film is about 2000 times smaller than that of the air it is measuring, implying that smectic films should be very sensitive to the velocity of air flowing over them. Smectic films are intrinsically much more stable than films of conventional fluids, lasting up to several years in the laboratory, and have been used previously to probe 2D hydrodynamics [?, ?] and rheology [?], shear-stress measurements [?], and in pressure metrology [?, ?]. The application described here uses smectic films for flow measurements.

When a film is first drawn, it is typically only a few smectic layers thick and appears uniformly black in reflected light. In the prototype racetrack geometry sketched in Fig. 4.1(a), air is then injected at a known volumetric flow rate into the continuous rectangular channel located beneath the film. The inlet airflow is independently monitored using a mass airflow sensor (Honeywell AWM5101VN) capable of measuring flow rates between 0 and 5 standard litres per minute (SLPM). As the air flows through the channel, it shear couples to the liquid crystal, causing circulation of the film around the racetrack. This flow typically pulls some additional LC material in from the meniscus, leading to the formation of small, disc-like islands embedded in the film. Since the reflectance of thin, freely-suspended films depends quadratically on thickness[?], the islands are brighter than the background film and can easily be visualized using video microscopy. The motion of the islands is observed on the “backstretch” of the racetrack using a  $5\times$  objective and captured using a high-speed video camera (Vision Research Phantom v12.1) at rates of 100–5000 frames per second. The islands are tracked using the open source Python library Trackpy [?], allowing us to use PTV methods [?, ?, ?, ?] to measure the velocity field of the film in the region of interest.

The device works by optically measuring the island velocity, which should be linearly coupled to the velocity of the airflow. In contrast to other mechanical flow meters, our flow

meter should thus be uniformly sensitive to airflow, regardless of the airflow velocity.

Our experimental approach has much in common with traditional PTV methods, where tracer particles are injected into the gas being measured and a light sheet created by a laser is used to define an illuminated plane, so that the tracer particles intersecting this plane can be tracked with a camera, mapping out the gas flow. A key difference is that our tracer particles (the islands) are embedded in a fluid with low vapor pressure ( $< 10^{-6}$  torr)[?] that couples hydrodynamically to the gas flow, rather than relying on solid particles introduced into the gas. In the LC flow meter, the gas thus remains free of foreign tracer particles, making this a useful, non-invasive approach for systems where maintaining gas purity is important.

## 4.2 Theory and Simulation

In order to act as an ideal mechanical flow meter, the LC device should couple linearly to the gas flow (i.e., with a sensitivity independent of flow velocity) while having a minimal effect on the system being measured.

Linearity is an intrinsic feature of this system because of the standard no-slip boundary condition between two fluids in contact. Because the velocity of the air varies over the height of the channel, the average air and film velocities will be slightly different.

In order to model the behavior of the LC flow meter, we first consider two-phase, stratified flow in an infinitely long, rectangular pipe with symmetry about the midplane, a geometry that is amenable to an analytic approach [?, ?].

The symmetric rectangular pipe has the essential elements of the racetrack flow meter, a multiphase system where a thin fluid is surrounded by air, but has none of the complicating geometrical factors, allowing us to focus on the intrinsic properties of the air and film interaction. By varying the relative volume of the air and liquid phases (the phase fraction), we can estimate the effect of a fluid with the same thickness as a freely suspended film on the airflow.

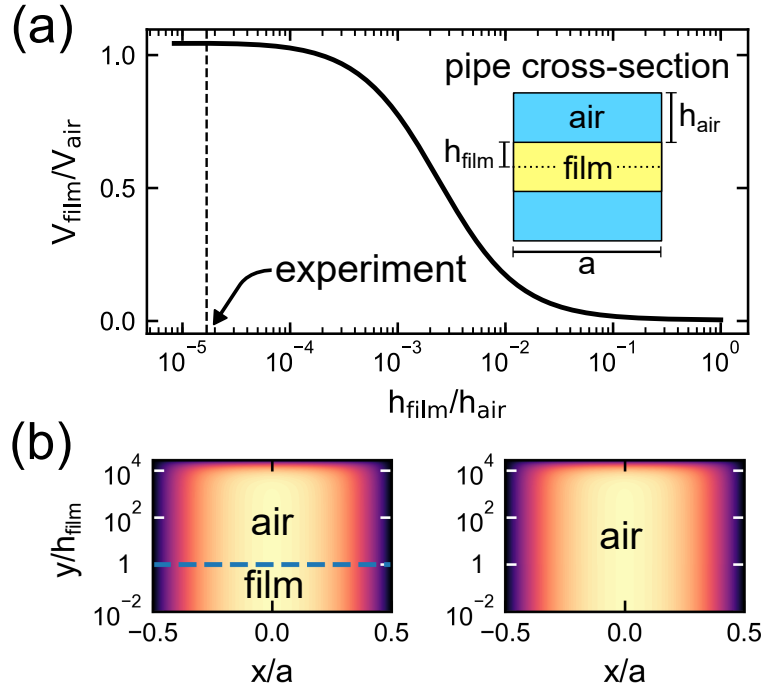


Figure 4.2: Analytic analysis of symmetric, two-phase, stratified fluid flow in an infinitely long pipe of width  $a$ . (a) Ratio between the average film and air velocities as a function of the phase fraction (the ratio of the volume of the fluid and the volume of the air,  $\phi = h_{\text{film}}/h_{\text{air}}$ ). When the phase fraction is very small, the film is strongly coupled to the air and moves with the same speed. (b) Flow velocity in the top half of the pipe. At left, both air and film are flowing through the pipe (the blue dashed line demarcates the upper boundary of the film), while on the right only air is present. The  $y$  dimension is scaled by the half the thickness of the LC film,  $h_{\text{film}}$ . The flow fields in these two cases are practically indistinguishable, suggesting that the influence of the LC film on the airflow is negligible.

We solved the Navier-Stokes equations to determine the airflow in the pipe both with and without the LC film, using appropriate viscosities for the air ( $1.8 \times 10^{-5}$  Pa s) and LC film ( $5.2 \times 10^{-2}$  Pa s)[?]. At values of the phase fraction corresponding to the experiment (with a thick LC film of 60 molecular layers,  $\phi \sim 10^{-5}$ ), the flow of the LC film is found to be coupled identically to that of the air (Fig. 4.2(a)). Furthermore, the air flow in the presence of the LC film is essentially indistinguishable from the flow in the absence of the film (Fig. 4.2(b)), suggesting that, at least in this idealized geometry, the film extracts a negligible amount of energy from the air flow. Details of these calculations are given in the Supplemental Information.

We numerically modeled the flow of air in the 3D racetrack geometry, without the liquid crystal film but choosing track dimensions and flow parameters consistent with our experiments.

Modeling the air flow alone allows us to see the “natural state” of flow in the racetrack geometry in the absence of the LC film. As the results of the analytical modeling in the previous section suggest that the film has a negligible influence on the airflow, we expect these airflow-only simulations to closely mimic the experimental behaviour.

The results of these simulations then allow us to see whether the geometry of the racetrack modifies the linear sensitivity predicted from the analytical model. We can also test the assumption that the film has a negligible impact on the overall flow behaviour by comparing the results of the air-flow simulations to the observed experimental flow behaviour.

The simulations were performed using OpenFOAM, an open-source fluid dynamics solver that uses a SIMPLE algorithm[?]. The results are summarized in Fig. 4.3 with further details given in the Supplemental Information. The simulations indicate that at low inlet velocity values ( $\lesssim 0.55$  m/s) the air stream in the channel splits, so that it flows in the same absolute direction along both arms of the racetrack. At  $v_{\text{in}} = 0.55$  m/s, the airflow is predicted to transition to homogeneous, clockwise circulation.

The net force on an LC film in contact with the air stream is the sum of the shear forces along the entire length of the racetrack, for which there are two main contributions: the air moving along the shortest distance from the inlet to the outlet (at speed  $v_2$ ), and the air moving along the other side of the racetrack (at speed  $v_1$ ). Because the LC film is incompressible, if  $v_1$  and  $v_2$  are in the same absolute direction, as in Fig. 4.3(a), then the steady state film velocity is  $v_{\text{film}} \propto v_2 - v_1$ . This predicted film speed is in general lower than but roughly proportional to the inlet air flow, as shown in Fig. 4.3(b).

We think that the chaotic flow we observe in the racetrack is a manifestation of the ‘split-flow’ predicted by the simulations. We hypothesize that the film acts to bias the air-film system to a circulating regime, explaining why the air-film onset to circulating flow happens

at lower inlet velocities than the simulations predict for pure airflow.

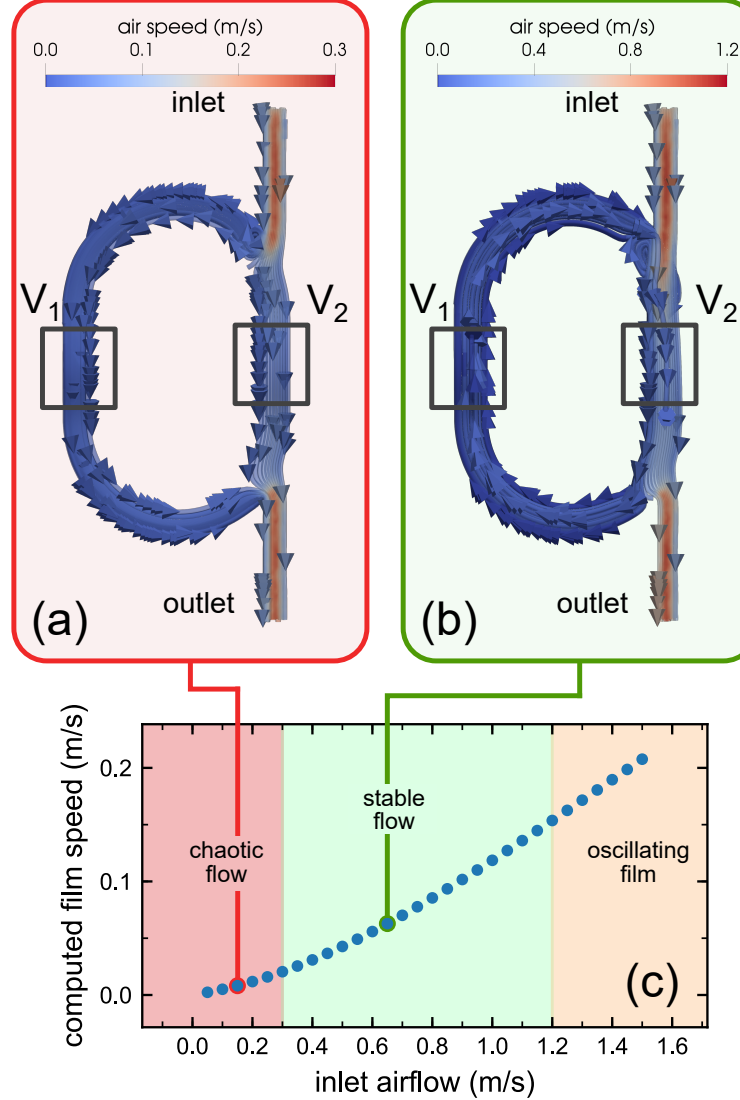


Figure 4.3: Computed airflow in the racetrack geometry. (a) Model velocity field for inlet velocity  $v_{\text{inlet}} = 0.15 \text{ m/s}$ . The air does not circulate uniformly in the same sense around the racetrack, instead splitting between the front and back legs. (b) Model velocity field for inlet velocity  $v_{\text{inlet}} = 0.65 \text{ m/s}$ . Above a transition inlet velocity of  $v_{\text{inlet}} = 0.55 \text{ m/s}$ , the air circulates uniformly around the racetrack. (c) Predicted net film speed ( $v_{\text{film}} \propto v_2 - v_1$ ) for a range of inlet velocities. The slope of this curve gives an average theoretical sensitivity of  $S = 0.15$ . The background shading reflects the experimental observations with different inlet velocities: for  $v_{\text{in}} < 0.3 \text{ m/s}$ , the film flow is chaotic; for  $0.3 \text{ m/s} < v_{\text{in}} < 1.2 \text{ m/s}$ , the film exhibits stable Poiseuille flow; for  $v_{\text{in}} > 1.2 \text{ m/s}$ , the film undergoes rapid out-of-plane oscillations that make particle tracking impractical.

In summary, the analytic and numerical models both suggest that freely-suspended LC

films in racetrack geometry should make excellent flow detectors, linearly coupling to and stabilizing the air flow.

### 4.3 Results and Discussion

We measured the velocity fields of LC films coupled to inlet airflows in the range 0.1 SLPM–0.4 SLPM. We observed three main regimes of film flow behaviour, indicated by the shading in Fig. 4.3(c). Below a threshold inlet air velocity ( $v_{\text{in}} < 0.3 \text{ m/s}$ ), the flow is characterized by time-dependent, chaotic behavior, with flow reversal and eddy currents observed in the films. This behavior is likely due to flow splitting of the type shown in Fig. 4.3(a), where the incoming air stream is divided between the short and long arms of the racetrack.

At intermediate air inlet velocities ( $0.3 \text{ m/s} < v_{\text{in}} < 1.2 \text{ m/s}$ ), the film undergoes uniform, counter-clockwise circulation around the racetrack, as shown in Fig. 4.4(a), with a Poiseuille flow profile across the film that stabilizes in less than 1 second. The observed threshold speed for the transition from chaotic flow to uniform circulation ( $v_{\text{in}} \sim 0.3 \text{ m/s}$ ) is somewhat lower than predicted by the simulations for airflow alone ( $v_{\text{in}} \sim 0.55 \text{ m/s}$ ). This suggests that the film acts to stabilize homogeneous flow, promoting a uniform, regular circulation of the film and air. Because our measurement relies on obtaining regular, simple flow, the stable regime is clearly optimal for operation of the flow meter, and extending the usable range to lower inlet velocities is a clear advantage of the LC film-air system. At high air inlet velocities ( $v_{\text{in}} > 1.2 \text{ m/s}$ ), the film oscillates rapidly up and down, causing the islands to go in and out of focus and the film eventually to break.

A comparison of the spatially averaged film speed measured half way along the back stretch of the racetrack to the independently measured inlet airflow is plotted in Fig. 4.4(b). The average slope of this graph gives a measured sensitivity of the flow meter of  $S = 0.09$ . This is slightly less than the sensitivity predicted from the pure airflow simulations, a difference

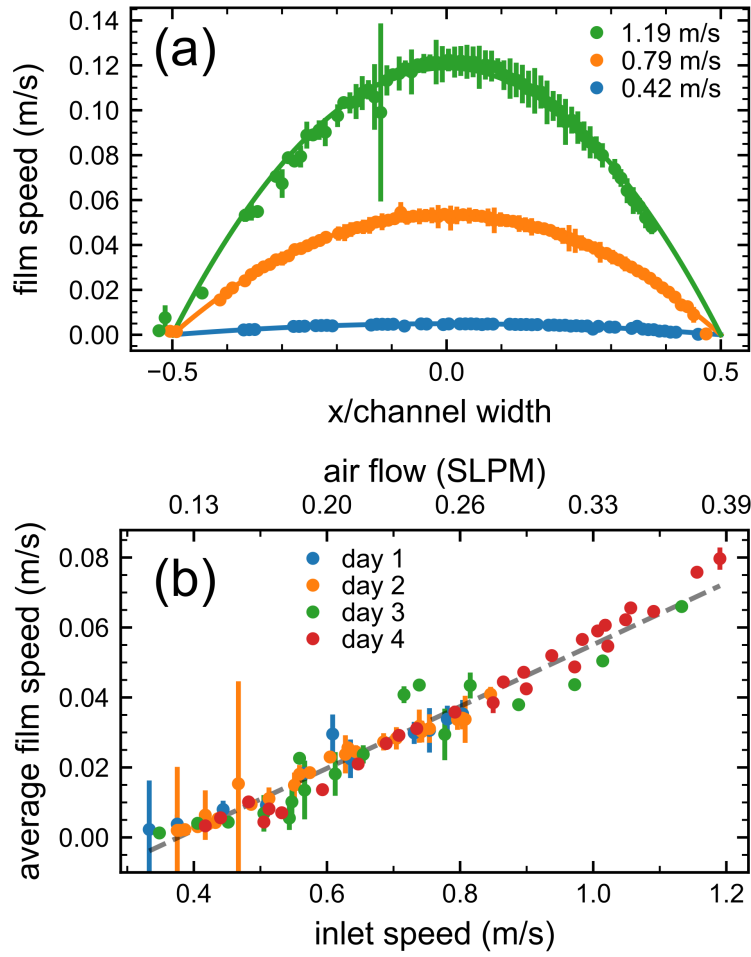


Figure 4.4: Characterization of flow meter. (a) Velocity profiles over the width of the racetrack channel, with each point corresponding to a specific tracked island. The profiles are well described by parabolas (smooth curves), confirming Poiseuille flow over a wide-range of inlet velocities. At higher velocities, the data are noisier due to the relatively paucity of islands that can be captured in sequential frames. The left-right asymmetry in the number of measurements is an artifact due to defects on one side of the camera sensor. (b) Spatially averaged film velocity in the observation region as a function of inlet air velocity. Measurements were performed over four separate days, using more than 30 films. The volumetric flow rate of the air being injected into the racetrack through the inlet was measured using an independent mechanical sensor. The average film speed is linearly proportional to the speed of the air at the device inlet, with a sensitivity that is independent of flow rate.

which we attribute to air loss during the air-injection process. With some refinement of the racetrack geometry, we would expect to extend the accessible measurement range to lower velocities. The upper velocity limit could be raised by implementing measures to equalize the air pressure across the film. We believe that such differences in air pressure are responsible for the rapid vertical oscillations observed at high flow rates.

By harnessing the unique properties of freely-suspended smectic films, we have demonstrated a method for mechanical measurement of air flow that has intrinsically linear sensitivity. This technique could usefully be applied to mapping the velocity field of gases flowing through exotic microfluidic geometries in two dimensions.